The Abdus Salam International Centre for Theoretical Physics

IAEA International Atomic Energy Agency

unesco United Nations Educational, Scientific and Cultural Organization

Workshop on Twistronics and Moiré Materials: Bridging Theory and Experiments | (SMR 3918)

16 Jan 2024 - 19 Jan 2024
ICTP, Trieste, Italy

P01 - BAÙ Nicolas

Local Chern Marker for Periodic Systems

P02 - BIDOGGIA Davide

Molecular Layers on Graphene: Exploring Lattice Periodicity through Theory-Experiment Synergy

P03 - CHOWDHURY Tamaghna

Stacking Engineered Room Temperature Ferroelectricity in Twisted Germanium Sulfide Nanowires.

P04 - DUBEY Ashutosh

Optical response of periodically driven twisted bilayer graphene and Dirac system

P05 - DUTTA Debasis

Novel interband plasmon and nonreciprocal responses in twisted multilayer graphene system

P06 - DUTTA Ranit

Electric Field Tunable Superconductivity in near Magic- Angle Twisted Bilayer Graphene

P07 - FAVATA Roberta

Topological phase diagram of two-band fermionic chain in presence of Hubbard interaction

P08 - FELISAZ Johan Claudius Jean-Paul

Effect of h-BN encapsulation on graphene systems: ab initio calculations and effective model

P09 - OTERO FUMEGA Adolfo

Moiré-driven multiferroic order in twisted Chromium trihalides

P10 - GHOSH Ayan

Enhanced thermopower and large magneto-resistance in compensated electron-hole bands of twisted double bilayer graphene

P11 - GUPTA Neelam

Ultralow lattice thermal conductivity and thermoelectric performance of twisted Graphene/Boron Nitride heterostructure through strain engineering

P12 - HADDAD Sonia

Twisted bilayer graphene reveals its flat bands under spin pumping

P13 - HERRERA GONZÁLEZ Saúl Antonio

Doped graphene superlattices: Flat bands and superconductivity without twists

P14 - ISHII Fumiyuki

First-Principles Study of Band Structure in Twisted Bilayer Graphene Flake using Band Unfolding Method

P15 - IZADI VISHKAYI Sahar

Moiré-induced bandgap tuning in InSe/CuSe heterostructure

P16 - JANKOWSKI Wojciech Jan

Topologically non-trivial polarization textures in moire materials

P17 - JIMENO-POZO Alejandro

Superconductivity from electronic interactions in few layers of graphene.

P18 - KUNDU Ritajit

Josephson junction of minimally twisted bilayer graphene

P19 - DE PAULA ALMEIDA LIMA Rodrigo

Electronic transport in collapsed chiral carbon nanotube

P20 - MANNAI Marwa

Stacking-induced Chern insulator

P21 - MOHAMMADIZADEH Mohammadreza

First-Principles Study of Hydrogen Dynamics in Monoclinic TiO

P22 - NAVARRO LABASTIDA Leonardo Antonio

3/2 magic angle quantization rule of flat bands and its relationship to the quantum Hall effect and localization centers of the electronic wave functions at high order magic angles in twisted bilayer graphene

P23 - CORREIA NINHOS Pedro António

Exciton-polaritons in an one-dimensional hexagonal boron nitride superlattice

P24 - PARRA MARTÍNEZ Guillermo

Electronic properties of twisted TMDs using Wannier based Tight-Binding model

P25 - PASQUA Ivan

Non-local correlations and exciton condensation in a model Quantum Spin Hall Insulator

P26 - PUTATUNDA Aditya

Magnetism in twisted bilayer Moiré systems from first-principles

P27 - RAI Gautam

Dynamical correlations and order in magic-angle twisted bilayer graphene

P28 - SAINZ-CRUZ Héctor

Mirror-protected Majorana zero modes in f-wave multilayer graphene superconductors

P29 - SHAH Muzamil

Proximity-induced topological phases in a twisted heterostructure of transition metal dichalcogenide and CrI3

P30 - SILVA Andrea

Moiré-driven depinning and emerging chirality in twisting crystalline interfaces

P31 - SINGH Arushi

Defect-driven tunable electronic and optical properties of two-dimensional silicon carbide

P32 - STAVRIC Srdan

Graphene striped moiré for 1D confinement and selective diffusion of metal atoms

P33 - SZENTPÉTERI Bálint

Stabilizing the inverted phase of a WSe2/BLG/WSe2 heterostructure via hydrostatic pressure

P01

Local Chern Marker for Periodic Systems

N. Baù[1], **A. Marrazzo**[1]

[1] *Università degli Studi di Trieste*

Topological invariants are global properties of the ground-state wave function, typically defined as winding numbers in reciprocal space. Over the years, a number of topological markers in real space have been introduced, allowing to map topological order in heterogeneous crystalline and disordered systems [1]. Notably, even if these formulations can be expressed in terms of lattice-periodic quantities, they can actually be deployed in open boundary conditions only, as in practice they require computing the position operator $\mathbf{r}$ which is ill-defined in periodic boundary conditions. We derive a local Chern marker for infinite two-dimensional systems with periodic boundary conditions in the large supercell limit, where the electronic structure is sampled with one single point in reciprocal space [2]. We validate our approach with tight-binding numerical simulations on the Haldane model, including trivial/topological superlattices made of pristine and disordered Chern insulators. The strategy introduced is very general and could be applied to other topological invariants and geometrical quantities in any dimension.

[1] Raffaello Bianco and Raffaele Resta Phys. Rev. B **84**, 241106(R) (2011).
[2] Davide Ceresoli and Raffaele Resta Phys. Rev. B **76**, 012405 (2007).

P02

Molecular Layers on Graphene: Exploring Lattice Periodicity through Theory-Experiment Synergy

Davide Bidoggia, Francesco Armillotta, Erik Vesselli, Maria Peressi

Self-assembled molecular adlayers on metallic surfaces represent a promising class of catalytic systems for heterogeneous catalysis. The periodicity of these adlayers is determined by the constituting molecules and by the substrate. The interplay between molecule-substrate and molecule-molecule interactions plays a critical role in determining the self-assembly process and the resulting pattern, which, in turn, determines the electronic and catalytic properties of the layer.

In some cases, the substrate plays a critical role and provides a template hosting the adsorbates in a selective way, or determining specific moiré patterns if the adsorbate has a periodicity different with respect to the substrate. In case of Cobalt tetrapyridil porphyrins (CoTPyP) adsorbed on graphene grown on an iridium (111) surface, the molecule-substrate interaction is rather weak: it affects only the rotation angle of the pyridinic termination with respect to a gas phase conformation, and an individual molecule does not have a preferential adsorption site or orientation with respect to the substrate. As a consequence, the intermolecular interactions dominate and the molecular layer assumes periodic patterns incommensurate with the substrate. The coincidence cells that must be used to describe such systems are typically quite large.

Using a combination of density functional theory and experimental investigations, we present some results on the geometric structure of the CoTPyP adlayers and its impact on electronic properties. We show, in particular, the significant surface reorganization upon the evaporation of additional Co atoms onto the surface.

P03

Stacking Engineered Room Temperature Ferroelectricity in Twisted Germanium Sulfide Nanowires

Tamaghna Chowdhury[1], **Chetna Tenja**[1], **Aastha Vasdev**[2], **Prasenjit Ghosh**[1], **Goutam Sheet**[2], **G. V. Pavan Kumar**[1] **and Atikur Rahman**[1]

[1] *Department of Physics, Indian Institute of Science Education and Research (IISER), Pune, Maharashtra 411008, India*

[2] *Department of Physical Sciences, Indian Institute of Science Education and Research, Mohali, Knowledge City, Sector 81, Mohali 140306, India*

Transition metal dichalcogenides (TMDC's) and group-IV monochalcogenides, with the potential to show piezoelectric and ferroelectric properties, have grown considerable interest in recent years. Ferroelectricity involves spontaneous electric polarization that can be tuned by an external electric field. Ferroelectricity in the group-IV monochalcogenides may be more advantageous, as such materials display additional features such as tunable band gap and flexibility that are crucial for applications as sensors and memory devices. Materials with broken inversion symmetry are expected to show ferroelectricity but many of the TMDCs and group-IV monochalcogenides in their bulk form have inversion symmetry that forbids spontaneous polarization[1]. However, if the inversion symmetry is broken then these materials might exhibit ferroelectricity[2]. Germanium sulfide (GeS) is one such material with inversion symmetry and lacks spontaneous polarization in its bulk form owing to its centrosymmetric crystal structure. In the fabrication of non-centrosymmetric GeS, the main challenge lies in the complexity of the preparation and assembly of GeS layers. One way to achieve that is by the introduction of twists. The fabrication of twisted nanostructures using the transfer stacking method is usually a very challenging task because of poor control over twist angle. Recently, a robust process to grow twisted GeS nanowires by introducing Eshelby twist between two adjacent layers was demonstrated [3, 4]. These nanowires are formed by stacking layers held together via vdW interaction along the transverse direction. We used GeS nanowires made of stacked layers as a model system and introduced Eshelby twist in consecutive layers to break the inversion symmetry. In the I–V characteristics of the nanowires, hysteresis, a characteristic feature of ferroelectric switching, was observed. The ferroelectric nature of these nanowires was further established by piezoresponse force microscopy (PFM) measurement and the nanowires exhibited spontaneous polarization also there is a 180° polarization switching in an external electric field at room temperature. Second-harmonic generation (SHG) measurement showed a strong signal from these twisted nanowires that confirmed the presence of broken inversion symmetry. Phonon dispersion of the nanowire was calculated using density functional theory (DFT) that showed the hardening of the inversion symmetry breaking phonon mode due to the twisting. But this induces an instability that is compensated by spreading the twist across several unit cells. This twist results in the breaking of the inversion symmetry that might induce a spontaneous polarization in the nanowire, giving rise to ferroelectricity[5]. These results are expected to be useful in making non-volatile memory devices, flexible electronics, electronic sensors, and neuromorphic computing.

[1] T. Rangel *et. al.*, Phys. Rev. Lett. **119**, 067402 (2017).
[2] R. Fei *et. al.*, Phys. Rev. Lett. **117**, 097601 (2016).
[3] Y. Liu *et. al.*, Nature **570**, 358 (2019).
[4] P. Sutter *et. al.*, Nature **570**, 354 (2019).
[5] T. Chowdhury *et. al.*, Adv. Elec. Mater. **8**, 2101158 (2022).

P04

Optical response of periodically driven twisted bilayer graphene and Dirac system

Ashutosh Dubey[1], **Ritaji Kundu**[1], **and Arijit Kundu**[1]

[1] *(Presenting author underlined) Indian Institute of Technology 1*

We compute, theoretically, the optical conductivity and ARPES response of periodically driven Dirac system(twisted bilayer graphene as well as semi-Dirac system), in identifying signatures of partial steady-state occupation of floquet bands. For a closed, periodically driven system, such occupation is determined by weakly coupling to an environment. We contrast this with occupation of Floquet bands when no relaxation is present.

P05

Title- Novel interband plasmon and nonreciprocal responses in twisted multilayer graphene system

Debasis Dutta*[1], Atasi Chakraborty[1] , Amit Agarwal[1]

[1]*Department of Physics, Indian Institute of Technology Kanpur, Kanpur-208016, India*

Email Address- ddebasis@iitk.ac.in

The optical responses of a metallic system are often described by plasmon resonances—the collective oscillations of interacting electron liquids. Here, I will discuss a new class of plasmon modes in moiré superlattices of twisted graphene multilayers (TGM). In TGM, the single-particle band dispersion dramatically changes compared to single-layer graphene due to the emergence of nearly flat bands, resulting from the moiré potential induced by twist. These flat bands enable nearly parallel electron-hole transitions in reciprocal spaces, effectively giving rise to an interband plasmon mode, even in insulating systems. Here, I demonstrate the existence of long-lived gapped interband plasmons in twisted double-bilayer graphene originating from the Van Hove singularity in the electron-hole joint density of states spectrum [see Fig.1 attached below]. Our finding highlights the universal dispersion of interband plasmon in the long-wavelength limit [1].

Along with that, I will also describe the emergence of the nonreciprocal plasmonic responses, which have different dispersion for forward and backward propagating modes in twisted bilayer graphene heterostructures [2]. Nonreciprocal plasmonics plays a crucial role in enabling one-way light propagation at the nanoscale and is a fundamental building block for various photonics applications. I will discuss how the quantum geometry of the Bloch states (e.g.- quantum metric, metric connection) in twisted bilayer graphene enables significant intrinsic nonreciprocity in bulk plasmon dispersion. This magnetic field-free nonreciprocal plasmon with a quantum origin opens a new avenue of optical manipulation at the nanoscale.

References-

[1] Atasi Chakraborty, Debasis Dutta, and Amit Agarwal, “Tunable interband and intraband plasmons in twisted double bilayer graphene,” Phys. Rev. B 106, 155422 (2022).

[2] Debasis Dutta, Atasi Chakraborty, Amit Agarwal- “Intrinsic nonreciprocal bulk plasmons in noncentrosymmetric magnetic systems” Phys. Rev. B, 107, 165404 (2023).

.

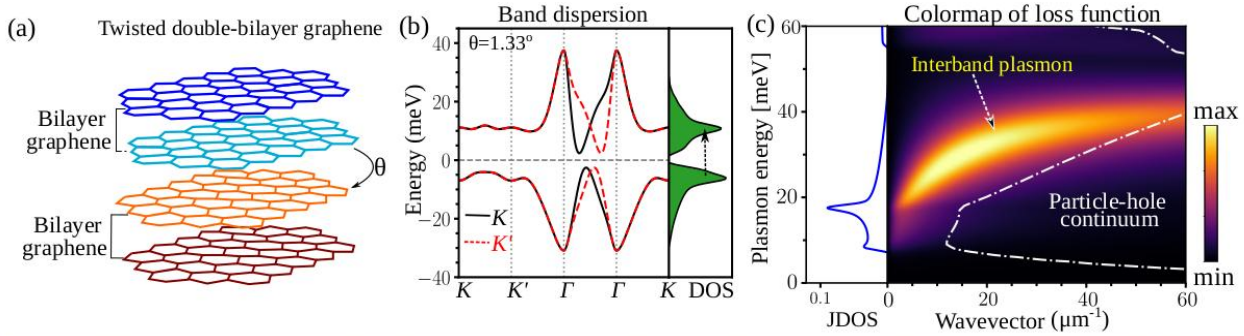

Figure-1- (a) Schematic of twisted double bilayer graphene structure, with small twist(θ) between two bilayer graphene. (b) The single-particle band structure of TDBG calculated from continuum model. It hosts two nearly flat bands, having van-Hove singularities in DOS spectrum. (c) The colormap of loss function spectrum, where plasmon modes appear as peaks. It captures the interband plasmon, staring from the peak in the joint density of states (JDOS) spectrum. The interband plasmon is long-lived and well outside the particle-hole continuum regions.

P06

Electric Field Tunable Superconductivity in near Magic-Angle Twisted Bilayer Graphene

Ranit Dutta[1*], Ayan Ghosh[1†], Shinjan Mandal[1] , K. Watanabe[2] , T. Taniguchi[3], H.R.Krishnamurthy[1], Sumilan Banerjee[1], Manish Jain[1], and Anindya Das[1‡]

[1]*Department of Physics, Indian Institute of Science, Bangalore, 560012, India.*
[2]*Research Center for Functional Materials, National Institute for MaterialsScience, Tsukuba, Japan.*
[3]*International Center for Material Nanoarchitectonics, National Institute for Materials Science, Tsukuba, Japan*

The cause of superconductivity (SC) in magic-angle twisted bilayer graphene (MATBLG) has been a topic of debate, with theories ranging from strong correlations (CL) like in high T_c cuprates to a high density of states-mediated electron-phonon coupling. Previous experimental studies with detuning from magic-angle as well as tuning the screening have shown that the SC and Correlated insulator may not have an intimate connection. However, one crucial ingredient, like how an insitu tuning of the electronic band structure affects the SC, is missing so far, and here we study this for a near MATBLG device ($\theta_M \approx 0.96^0$) with the application of displacement field (D). In this device, we observe the resistance peaks at the Dirac point and at band full filling without any signature CL-driven resistance peaks, and the SC appears around $\nu = 2.7$. Simultaneously, measuring the SC critical temperature (T_c) and Hall density, ν_H as a function of D, helps us to study the intimate connection between the SC and electronic structure of TBLG. We observe the optimal doping for SC, and vHS appears concomitantly, and with increasing D, both shift to higher filling. The shift of vHS with D is further captured in our theoretical study due to the band structure modification. Most importantly, the T_c is tunable with D; it decreases from 0.80 K to 0.55 K by increasing the D from zero to $D = 0.60V/nm$; beyond which it is hard to see any signature of SC. Furthermore, the weakening of SC with increasing D is accompanied by a reduction of hall-filling ν_H, and the appearance of a resistance peak around $\nu = 2$ suggests that isospin symmetry is breaking and competing with the SC. Our results bring new insights into understanding the SC phase in the TBLG system.

*equally contributed
†equally contributed
‡anindya@iisc.ac.in

P07

Topological phase diagram of two-band fermionic chain in presence of Hubbard interaction

R. Favata[1], **F. Becca**[1], **and A. Parola**[2]

[1] *Dipartimento di Fisica, Università di Trieste, Strada Costiera 11, I-34151 Trieste, Italy*
[2] *Dipartimento di Scienza e Alta Tecnologia, Università dell'Insubria, Via Valleggio 11, I-22100 Como, Italy*

We explore the ground-state properties of a two-band fermionic chain supporting a symmetry-protected topological insulator phase, in the presence of Hubbard interaction, inspired by the model proposed in [1]. Starting from the non-interacting ground state, we define a two-orbital Jastrow-Slater wave function which provides a proper variational description of the topological phase diagram. The topological phase transition, which is controlled by the on-site term only, is shifted to greater values of the parameter, with respect to the non-interacting limit, as the repulsion U between electrons on the same orbital is increased. The topological properties in presence of interaction are detected by the many-body marker introduced by Resta and Sorella [2]. Furthermore, the topological non-trivial behaviour of the system persists in the large U limit, where the spin-1 Haldane chain, characterized by string order, emerges as effective spin Hamiltonian.

[1] S. Barbarino, G. Sangiovanni, and J. C. Budich, Phys. Rev. B **99**, 075158 (2019).
[2] R. Resta and S. Sorella, Phys. Rev. Lett. **82**, 370 (1999).

P08

Effect of h-BN encapsulation on graphene systems: ab initio calculations and effective model

J. Félisaz[1], **O. V. Yazyev**[1]

[1] *École Polytechnique Fédérale de Lausanne (EPFL), Switzerland*

The substrate or encapsulation as a strong effect on the electronic structure of graphene systems. However, due to a lack of proper understanding of these effects, it has proven difficult to include them properly in twisted system models. In order to describe the effect of the substrate in a more systematic way, extensive DFT calculations were conducted for a large number of configurations. From these, a family of tight-binding (TB) models is constructed, dependent on the relative displacement between the graphene and h-BN layers. These models are designed to respect the symmetries of the various configurations. Substrate-aware models are constructed for moiré systems, including both small twist angles and graphene/h-BN lattice mismatch in the limit of large moiré lattice periods. We show that our framework is general enough to be applied to other systems, including moiré systems with lattice reconstruction, polar domains, and disordered substrates.

P09

Moiré-driven multiferroic order in twisted Chromium trihalides

Adolfo O. Fumega [1] , **Jose L. Lado** [1]

[1] *Department of Applied Physics, Aalto University, FI-00076 Aalto, Finland*

Layered van der Waals compounds have revolutionized the artificial design of materials. The unique degrees of freedom offered by this class of materials allow new strategies to engineer states of matter. In particular, the weak van der Waals interlayer bonding enables the introduction of a specific twist angle between the layers.

In this presentation we will show how to artificially engineer a multiferroic order using twisted chromium trihalide CrX_3 (X=Cl, Br, and I) bilayers [1]. The theoretical analysis introduced here is performed using a combination of spin models and ab initio calculations.
Firstly, we show the emergence of a spin texture as a result of the site-dependent interlayer magnetic exchange created by the moiré. The presence of spin-orbit coupling combined with that emergent non-collinear magnetic order induces an electric polarization and a strong magnetoelectric coupling in the system.
Among the three chromium trihalides, we found that $CrBr_3$ displays the strongest multiferroic order. We show that its magnetoelectric coupling allows us to electrically tune the magnetic texture of the moiré system. Specifically, we show that it is possible to generate and control magnetic skyrmions in twisted $CrBr_3$ with an external electric field.

[1] Adolfo O Fumega and Jose L Lado, *2D Mater.* 10 025026 (2023).

P10

Enhanced Thermopower and Large Magneto- resistance in Compensated Electron-hole Bands of Twisted Double Bilayer Graphene

Ayan Ghosh[1], Souvik Chakraborty[1], Unmesh Ghorai[2], Arup Kumar Paul[1], K. Watanabe[3], T. Taniguchi[3], Rajdeep Sensarma[2], and Anindya Das[1]*

[1]*Department of Physics, Indian Institute of Science, Bangalore, 560012, India.*
[2]*Department of Theoretical Physics, Tata Institute of Fundamental Research, Mumbai, 400005, India*
[3]*National Institute of Material Science, 1-1 Namiki, Tsukuba 305-0044, Japan*

*E-mail: anindya@iisc.ac.in

Finding materials with large thermopower has been crucial for envisioning development of novel electric generators and solid-state cooling devices. Recent advances have established semimetals to be a viable platform in this regard. Low-magnetic field-induced enhancement of thermopower has been theoretically predicted for compensated semimetals. Thus, exploring materials with semimetallic traits has been of increasing interest. Here, we report indisputable evidence of semi-metallic low energy band in twisted double bilayer graphene (TDBLG) with twist angle 1.2°. We have carried out a systematic temperature and magnetic field dependent electrical and thermopower study. An enhancement of two orders of magnitude of thermopower, accompanied by large magneto-resistance (~2500%), is observed near the charge neutrality point (CNP). Both the thermopower and magnetoresistance saturates within magnetic fields (< 1T) much smaller than the extreme quantum limit. These experimental findings indicate the nearly compensated semimetallic nature of TDBLG at the CNP, and qualitatively understood invoking a two-band model. Furthermore, we observe an unusual sub-linear temperature scaling of resistance at lower temperature (<10K) near the theoretically predicted region of overlap of the low-energy bands, indicative of a possible excitonic bound state in TDBLG.

P11

Ultralow lattice thermal conductivity and thermoelectric performance of twisted Graphene/Boron Nitride heterostructure through strain engineering

Neelam Gupta [1], Shivani Rani [1], Puja Kumari [1], Rajiv Ahuja[2,3], Soumya Jyoti ray[1,*]

[1]Department of Physics, Indian Institute of Technology Patna, Bihta 801103, India 1

[2] Department of Physics, Indian Institute of Technology Ropar, Rupnagar, Punjab 140001, India 2

[3] Condensed Matter Theory Group, Department of Physics and Astronomy, Uppsala University, SE-75120, Sweden 3

We designed and investigated the electronic, mechanical, and thermoelectric properties of Graphene/hexagonal Boron Nitride (Gr/h-BN) heterostructure at various twisting angles based on the Ab-initio simulation. The structural stability was studied at optimized rotation angle (ϕ) = 0º, 16.10º, 21.79º, 38.21º, 43.90º, and 60º. The heterostructure shows semiconducting nature at ϕ = 0º, 21.79º, and 38.21º. These twisted heterostructures have demonstrated extraordinary mechanical properties such as Young's modulus and bulk modulus. Using the semiclassical Boltzmann transport theory, it is observed that the Seebeck coefficient, electric conductivity, and power factor at ϕ = 0º, 21.79º, 38.21º, and 60º are much higher than the values measured at ϕ =16.10º and 43.90º. Moreover, at ϕ = 60º, the Power Factor for the n-type dopants can reach 1.37×10^{11} W/msK^2. The lattice thermal conductivity at room temperature is found to be very low for ϕ =16.10º, 21.79º, 43.90º, and 38.21º rotation angles. An ultralow lattice thermal conductivity with a value of 0.095 W/mK at 300K has been observed for 21.79º rotation angle, which is lower than other rotation angles because of very low group velocity (22.1 km/s) and short phonon lifetime (∼0.12 ps). The high thermoelectric performance results from an ultralow thermal conductivity arising due to the strong lattice anharmonicity. The present observations can offer significant impact on the design of high performance thermoelectric materials based on twisted van der Waals heterostructure (vdWH).

[1] Xiaoliang Zhong, Yoke Khin Yap, Physical Review B, **83**, 193403 (2011)

[2] Chun-Chung Chen, Zhen Li, Nano Research, **8**, 666—672 (2015)

P12

Twisted bilayer graphene reveals its flat bands under spin pumping

Sonia Haddad[1,2], **Takeo Kato**[3], **Jihang Zhu**[4], **and Lassaad Mandhour**[1]

[1] *Laboratoire de Physique de la Matire Condense, Facult des Sciences de Tunis, Universit Tunis El Manar,Campus Universitaire 1060 Tunis, Tunisia*

[2] *Institute for Theoretical Solid State Physics, IFW, Helmholtzstr. 20, 01069 Dresden, Germany*

[3] *Institute for Solid State Physics, University of Tokyo, Kashiwa, Chiba 277-8581, Japan*

[4] *Max Planck Institute for the Physics of Complex Systems, Nthnitzer Strasse 38, Dresden 01187, Germany*

The salient property of the electronic band structure of twisted bilayer graphene (TBG), at the so-called magicangle (MA), is the emergence of flat bands around the charge neutrality point. These bands are associated with theobserved superconducting phases and the correlated insulating states. Scanning tunneling microscopy combinedwith angle resolved photoemission spectroscopy are usually used to visualize the flatness of the band structureof TBG at the MA. Here, we theoretically argue that spin pumping (SP) provides a direct probe of the flat bandsof TBG and an accurate determination of the MA. We consider a junction separating a ferromagnetic insulatorand a heterostructure of TBG adjacent to a monolayer of a transition metal dichalcogenide. We show that theGilbert damping of the ferromagnetic resonance experiment, through this junction, depends on the twist angleof TBG, and exhibits a sharp drop at the MA. We discuss the experimental realization of our results which openthe way to a twist switchable spintronics in twisted van der Waals heterostructures [1].

[1] Sonia Haddad, Takeo Kato, Jihang Zhu, and Lassaad Mandhour, Phys. Rev. B **108**, L121101 (2023).

P13

Doped graphene superlattices: Flat bands and superconductivity without twists

Saúl A. Herrera [1], Pierre A. Pantaleón [2], G. Parra-Martinez[2], JA Silva-Guillen[2], Francisco Guinea[2,3], Gerardo G. Naumis[1]

[1]Instituto de Física, Universidad Nacional Autónoma de México, CDMX, México
[2]IMDEA Nanoscience, Madrid, Spain
[3]Donostia International Physics Center, San Sebastian, Spain

The properties of graphene can be substantially altered by periodic modulations induced via twists, strain, patterned gates, or by ad-atom deposition/intercalation. It has been shown that upon decoration with alkali metals, graphene can develop coupling between valleys [1], flat electronic bands [2], superconductivity [3], and other features resembling those of twisted multilayers. We discuss a relation between $\sqrt{3} \times \sqrt{3}$-patterned monolayers and chiral twisted bilayers. We also revisit the idea of using decoration/intercalation with metals to induce flat bands, strong screening and superconductivity without twists.

[1] Bao et al. PRL 126, 206804 (2021)
[2] Bao et al. PRB 105, L161106 (2022)
[3] B. M. Ludbrook et al. PNAS 112 (38) 11795-11799 (2015)

P14

First-Principles Study of Band Structure in Twisted Bilayer Graphene Flake using Band Unfolding Method

Wardah Amalia[1], Naoya Yamaguchi[2], Fumiyuki Ishii[2]

[1] Graduate School of Natural Science and Technology, Kanazawa University
[2] Nanomaterials Research Institute (NanoMaRi), Kanazawa University
e-mail: ishii@cphys.s.kanazawa-u.ac.jp

Twisted materials have attracted significant attention ever since the discovery of superconductivity in twisted bilayer graphene (BLG). Historically, most research on twisted materials has revolved around commensurate superlattices with extended periodicities. Remarkably, experimental success has been achieved in growing quasicrystals with a 30-degree twist in BLG, showcasing the potential for creating incommensurate structures under specific substrate conditions [1].

In this study, our primary objective is to ascertain whether we can reproduce the electronic structure of twisted BLG in finite-sized graphene flakes at specific commensurate twist angles that can be simulated using Density Functional Theory (DFT) calculations. We have conducted first-principles computations [2] on finite graphene structures, relaxing the constraints associated with commensurate arrangements. Consequently, we are able to continuously vary the interlayer rotation angles within the range of θ=6 degrees to θ=60 degrees and examine how the electronic properties are altered in these incommensurate structures, utilizing the unfolding band method [3]. It's worth noting that our methodology can be applied to various twisted bilayer systems.

Reference
1) W. Yao, et al. PNAS **115,** 27 (2018).
2) T. Ozaki et al., http://www.openmx-square.org.
3) C-C. Lee, Y. Yamada-Takamura, T. Ozaki, J. Phys.: Condens. Matter **25,** 345501 (2013).

P15

Moiré-induced bandgap tuning in InSe/CuSe heterostructure

S. I. Vishkayi [1] , M. B. Tagani [2] , B. Li [3], Y. Yang [3], J. Wang [3], Q. Tian [3], C. Zhang [3], L. Zhang [3], L. J. Yin [3], Y. Tian [3], L. Zhang [3], and Z. Qin [3]

[1] *School of Physics, Institute for Research in Fundamental Sciences (IPM), P. O. Box 19395-5531, Tehran, Iran*

[2] *Department of Physics, University of Guilan, P.O. Box 41335-1914, Rasht, Iran*

[3] *Key Laboratory for Micro/Nano Optoelectronic Devices of Ministry of Education & Hunan Provincial Key Laboratory of Low-Dimensional Structural Physics and Devices, School of Physics and Electronics, Hunan University, Changsha 410082, China*

The stacked two layered materials with a lattice constant mismatch and/or with a twist angle relative to each other can create a moiré pattern, modulating electronic properties of pristine materials. Optical properties of InSe and Dirac nodal lines in CuSe band structure motivated us to investigate the electronic properties of the moiré super lattice of InSe/CuSe heterostructure. In this work, a heterostructure with a super lattice periodicity of 3.48 nm and a twist angle of about 11° between InSe and CuSe layer was synthesized. The schematic of heterostructure is shown in Figure 1 (a). Scanning tunnelling spectroscopy recorded on the different stacking sites of the heterostructure reveals the bandgap of the InSe is location-dependent and a variation of 400 meV is observed. Density functional theory calculations demonstrate that the moiré-induce electric dipole in the monolayer InSe is the key factor for tuning the bandgap. Moreover, charge transfer between CuSe and InSe also contributes to the bandgap variation due to its stacking which is shown in Figure 1 (b) and (c). We also show that the moiré potential not only can tune the bandgap of InSe but also can vanish the Dirac nodal line of CuSe in some cases [1].

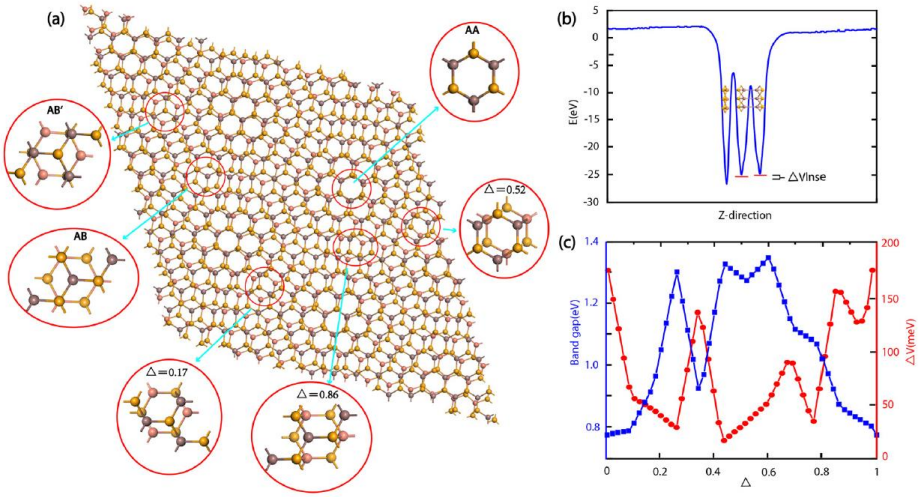

Figure 1, (a) moiré pattern of CuSe/InSe heterostructure. Some local moiré stackings are magnified for more clarity. The size of moiré is equal to 6.27×6.27 nm^2. Δ denotes the value of sliding monolayer InSe on CuSe in terms of lattice constant. (b) Electrostatic potential of the InSe/CuSe heterobilayer along the z-direction for AB stacking. The potential difference between the InSe layers is denoted by ΔV_{InSe}. (c) Variation of bandgap of monolayer with a lateral shift shown by blue squares. In addition, potential difference between two layers of InSe is also shown by red spots [1].

[1] B. Li, M. B. Tagani, S. I. Vishkayi, Y. Yang, J. Wang, Q. Tian, C. Zhang, L. Zhang, L. J. Yin, Y. Tian, L. Zhang, Z. Qin, Appl. Phys. Lett. **122,** 031902 (2023).

P16

Topologically non-trivial polarization textures in moiré materials

Wojciech J. Jankowski[1], D. Bennett[1,2], G. Chaudhary[1], E. Kaxiras[2,3], R.-J. Slager[1]

[1] Theory of Condensed Matter Group, Cavendish Laboratory, University of Cambridge, J. J. Thomson Avenue, Cambridge CB3 0HE, United Kingdom
[2] John A. Paulson School of Engineering and Applied Sciences, Harvard University, Cambridge, Massachusetts 02138, USA
[3] Department of Physics, Harvard University, Cambridge, Massachusetts 02138, United States

The modern theory of polarization provides a recipe for deducing the total polarization in a unit cell of any insulating system subject to periodic boundary conditions [1]. However, it cannot describe the local variation of polarization in a crystal supercell, which is important for understanding topologically non-trivial polarization textures observed in perovskite nanostructures [2] and moiré heterostructures formed by hexagonal boron nitride (hBN) or transition metal dichalcogenides [3]. While approximations to the local polarization in perovskite supercells have been used to successfully predict polar vortices and topological structures therein, these approximations are not valid in twisted bilayers, where the dynamical charges vary non-linearly throughout the supercell, forming polarization textures analogous to magnetic merons and skyrmions [3]. In this work, we show how the local polarization can be rigorously defined on the scale of single-layer unit cells as a gauge-invariant quantity [4]. We demonstrate how local polarization can be evaluated, circumventing the necessity of computing Berry phases for the total polarization of a supercell, using configuration space approximations. Furthermore, we illustrate the applications of the introduced definition of local polarization beyond the use of such approximations, in a continuum Bistritzer-MacDonald (BM) model [5] and effective 1D models with introduced superlattice periodicity.

[1] D. Vanderbilt and R. D. King-Smith, Phys. Rev. B 48, 4442 (1993).
[2] J. Junquera, Y. Nahas, S. Prokhorenko, L. Bellaiche, J. Iniguez, D. G. Schlom, L.-Q. Chen, S. Salahuddin, D. A. Muller, L. W. Martin, and R. Ramesh, Rev. Mod. Phys. 95, 025001 (2023).
[3] D. Bennett, G. Chaudhary, R.-J. Slager, E. Bousquet, and P. Ghosez, Nat. Comm. 14, 1629 (2023).
[4] D. Bennett, W. J. Jankowski, G. Chaudhary, E. Kaxiras, and R.-J. Slager, Phys. Rev. Research 5, 033216, (2023).
[5] R. Bistritzer and A. H. MacDonald, PNAS 108, 12233–12237 (2011).

P17

Superconductivity from electronic interactions in few layers of graphene.

Alejandro Jimeno-Pozo [1] , Héctor Sáinz-Cruz [1] , Tommaso Cea [1, 2] , Pierre A. Pantaleón[1] Vo T. Phong[3] , Ziyan Li[1, 4], Xueheng Kuang[1, 4], Zhen Zhan[1, 4], Min Long[1, 5] , Shengjun Yuan[4, 6] and Francisco Guinea[1, 7]

[1] IMDEA Nanoscience, C/Faraday 9, 28049 Madrid, Spain .

[2] Department of Physical and Chemical Sciences, University of L'Aquila, 67100 L'Aquila, Italy.

[3] Department of Physics and Astronomy, University of Pennsylvania, Philadelphia, PA, USA.

[4] Key Laboratory of Artificial Micro and Nano-structures of the Ministry of Education and School of Physics and Technology, Wuhan U niversity, Wuhan 430072, China.

[5] Department of Physics and HKU-UCAS Joint Institute of Theoretical and Computational Physics, The University of Hong Kong, Pokfulam Road, Hong Kong SAR, China.

[6] Wuhan Institute of Quantum Technology, Wuhan 430206, China.

[7] Donostia International Physics Center, Paseo Manuel de Lardizabal 4, 20018 San Sebastian, Spain.

The recent observation of superconductivity in both non-twisted and twisted few layers of graphene has ignited a enormous interest in unveiling the underlaying mechanism, as well as, wheter this mechanism is common to twisted and non-twisted structures. Here, we present a robust framework based on the Kohn-Luttinger mechanism able to capture the experimental phenomenology in both twisted and non-twisted systems. The superconducting instability is driven by the screened Coulomb interaction that becomes attractive under certain conditions. We find that superconductivity can be enchanced by the effect of Ising spin-orbit coupling and by strain in non-twisted graphene. For moiré systems we find that the complexity of the wavefunctions an the so-called Umklapp processes are crucial to achieve a critical temperature of the order of ~ 2 K. These calculations suggest that the Kohn-Luttinger mechanism, driven by electronic interactions, plays a significant role in superconductivity in both twisted and non-twisted graphene structures.

[1] A. Jimeno-Pozo, H. Sáinz-Cruz, T. Cea, P. A. Pantaleón and F. Guinea. Phys. Rev. B **107**, L161106 (2023).

[2] P. A. Pantaleón, A. Jimeno-Pozo, H. Sáinz-Cruz, V. T. Phong, T. Cea, and F. Guinea. Nat. Rev. Physics **5**, 304–315 (2023).

[3] Z. Li, X. Kuang, A. Jimeno-Pozo, H. Sáinz-Cruz, Z. Zhan, S. Yuan and F. Guinea. Phys. Rev. B **108**, 045404 (2023).

[4] M. Long, A. Jimeno-Pozo, H. Sáinz-Cruz, P. A. Pantaleón and F. Guinea. *In preparation.*

P18

Josephson junction of minimally twisted bilayer graphene

Ritajit Kundu[1], **Arijit Kundu**[1]

[1] *Department of Physics, Indian Institute of Technology Kanpur, Kanpur 208016, India*

At very small angles, the twisted bilayer graphene undergoes atomic reconstruction via local twisting and untwisting and breaks into triangular domains of AB and BA-stacked regions. The gate voltage can gap out the interior of the domains, leaving only the gapless domain wall modes at low energy. Depending on the model parameters, it has been demonstrated that such a system exhibits zigzag modes and pseudo-Landau levels. We investigate the signature of these modes in transport properties in a Josephson junction in which the normal region is composed of minimally twisted bilayer graphene (MTBG). In this regard, we employ the network model of MTBG, in which the propagating domain wall modes form the network's edges and the AA-stacked regions form its nodes. We characterise the transport signatures of the SNS junction in terms of the DC and AC Josephson effects and show that the zig-zag modes and the pseudo-Landau level have contrasting characteristics.

P19

Electronic transport in collapsed chiral carbon nanotube

Rodrigo P. A. Lima[1,2], **Olga Arroyo-Gascón** [1], **and Leonor Chico**[1]

[1] *GISC, Departamento de Física de Materiales, Universidad Complutense, E-28040 Madrid, Spain*

[2] *GFTC, Instituto de Física, Universidade Federal de Alagoas, Maceió AL 57072-970, Brazil*

We study the transport properties of a collapsed chiral carbon nanotube[1] contacted by two kinds of deformed carbon nanotube that act as leads. We analyze the conductance in terms of the spectra of the collapsed chiral carbon nanotube (see figure 1) and the contacts.

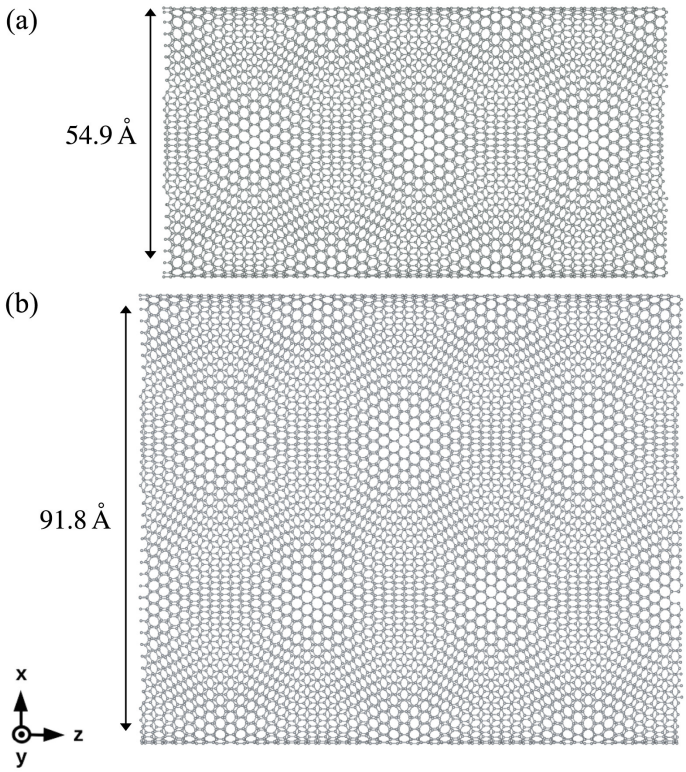

Figure 1: Top view of the unit cells of the (a) collapsed semiconducting (48,2) and (b) Γ-metal (78,3) nanotubes[2]. The number and placement of the AA regions differ and depend on the symmetry operations of the original cylindrical tube.

[1] Arroyo-Gascón, Olga and Fernández-Perea, Ricardo and Suárez Morell, Eric and Cabrillo, Carlos and Chico, Leonor, Nano Letters **20**, 7588 (2020).

[2] Olga Arroyo-Gascón and Ricardo Fernández-Perea and Eric Suárez Morell and Carlos Cabrillo and Leonor Chico, Carbon **205** 394 (2023).

P20

Stacking-induced Chern insulator

Marwa Mannaï[1,2], Jean-Noël Fuchs[3], Frédéric Piéchon[4], and Sonia Haddad[1,5]

[1]Laboratoire de Physique de la Matière Condensée, Faculté des Sciences de Tunis, Université Tunis El Manar, Campus Universitaire 1060 Tunis, Tunisia
[2]Center for Quantum and Topological Systems, New York University Abu Dhabi, United Arab Emirates.
[3]Sorbonne Université, CNRS, Laboratoire de Physique Th´eorique de la Matière Condensée, LPTMC, 75005 Paris, France
[4]Université Paris-Saclay, CNRS, Laboratoire de Physique des Solides, 91405, Orsay, France
[5]Institute for Solid State Physics, University of Tokyo, Kashiwa, Chiba 277-8581, Japan

Abstract

Graphene can be turned into a semimetal with broken time-reversal symmetry by adding a valley-dependent pseudo-scalar potential that shifts the Dirac point energies in opposite directions, as in the modified Haldane model. We consider a bilayer obtained by stacking two time-reversed copies of the modified Haldane model, where conduction and valence bands cross to give rise to a nodal line in each valleys. In the AB stacking, the interlayer hopping lifts the degeneracy of the nodal lines and induces a band repulsion, leading surprisingly to a chiral insulator with a Chern number $C = \pm 2$. As a consequence, a pair of chiral edge states appears at the boundaries of a ribbon bilayer geometry. In contrast, the AA stacking does not show nontrivial topological phases. We discuss possible experimental implementations of our results.

Motivation: Topology & Stacking

PHYSICAL REVIEW B **103**, 224304 (2021)

Bilayer Haldane system: Topological characterization and adiabatic passages connecting Chern phases

Sourav Bhattacharjee[1,*] Souvik Bandyopadhyay[1] Diptiman Sen[2] and Amit Dutta[1]
[1]*Department of Physics, Indian Institute of Technology Kanpur, Kanpur 208016, India*
[2]*Centre for High Energy Physics and Department of Physics, Indian Institute of Science, Bengaluru 560012, India*

Total Chern number of the bilayer Haldane model is $C_T = C_1 + C_2$ where C_l is the Chern number of each layer. In particular, Kane-Mele model amounts to stacking two opposite TRS copies of spin polarized Haldane model.

Recently, a modified Haldane model (mHM) has been proposed based on the Haldane model where the next-nearest-neighbor hopping term was introduced to act equally in both sublattices. The system turns into a semi-metal with a Fermi surface consisting, at half filling, of a hole pocket, in a valley, and an equal-sized electron pocket in the opposite valley. The so-called antichiral edge states are expected to emerge in zigzag nanoribbons described by the mHM: they are unidirectional gapless edge modes that co-propagate at the opposite ribbon boundaries and are counterbalanced by bulk states.

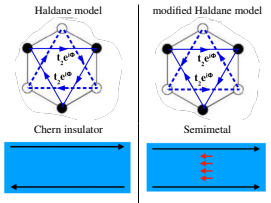

What about stacking two layers of mHM with undefined Chern number?

References

[1] E. Colomés and M. Franz.
Phys. Rev. Lett., 120(086603), 2018.

Modified Haldane model in AB bilayer: the model

Monolayer modified Haldane model

$$H(\mathbf{k}) = \left(\mathbf{a_k} + \mathbf{a_k^0}\right)\sigma_0 + \mathbf{b_k}\sigma_x + \mathbf{c_k}\sigma_y + \mathbf{M}\sigma_z$$

AB stacked mHM where the semimetallic layers break TRS in opposite ways

$$H_B(\mathbf{k}) = \begin{pmatrix} A_{1,\mathbf{k}} + M_1 & f_\mathbf{k} & 0 & 2t_\perp \\ f_\mathbf{k}^* & A_{1,\mathbf{k}} - M_1 & 0 & 0 \\ 0 & 0 & A_{2,\mathbf{k}} + M_2 & f_\mathbf{k} \\ 2t_\perp & 0 & f_\mathbf{k}^* & A_{2,\mathbf{k}} + M_2 \end{pmatrix}$$

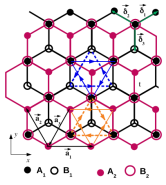

$2t_\perp$ is the interlayer coupling between dimer sites (A_1, B_2).

M_l $(l = 1, 2)$ is the layer Semenoff mass.

$b_\mathbf{k} = \Re\left(f_\mathbf{k}\right)$, $c_\mathbf{k} = -\Im\left(f_\mathbf{k}\right)$ with $f_\mathbf{k} = t\sum_{i=1}^{3} e^{i\mathbf{k}\delta_i}$

$A_{l,\mathbf{k}} = a_{l,\mathbf{k}} + a^0_{l,\mathbf{k}}$ where $\begin{cases} a_{l,\mathbf{k}} = -2t_2 \sin\Phi_l \sum_{i=1}^{3} \sin\left(\mathbf{ka_i}\right) \\ a^0_{l,\mathbf{k}} = -2t_2 \cos\Phi_l \sum_{i=1}^{3} \cos\left(\mathbf{ka_i}\right) \end{cases}$

Symmetries: $H_B(\mathbf{k})$ breaks TRS, $\mathcal{T} = K$, the charge conjugation, $\mathcal{C} = \sigma_z\tau_0 K$ and the chirality $\mathcal{S} = \tau_0\sigma_z$, meaning that the system belongs to class A labeled by a Z invariant.

Band structure:

$$\Delta_\mathbf{k} = E_{+,-} - E_{-,-} = 2\sqrt{A_\mathbf{k} - B_\mathbf{k}}$$

$A_\mathbf{k} = a_\mathbf{k}^2 + |f_\mathbf{k}|^2 + 4t_\perp^2$ and $B_\mathbf{k} = 2\sqrt{|f_\mathbf{k}|^2\left(a_\mathbf{k}^2 + t_\perp^2\right) + t_\perp^4}$.

gap closing condition $\Delta_\mathbf{k} = 0$ if

$\begin{cases} a_\mathbf{k} = 0 \rightarrow \text{Quadratic point (AB bilayer)} \\ t_\perp = \quad 0 \rightarrow \text{Nodal lines} \end{cases}$

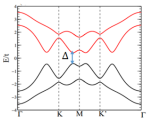

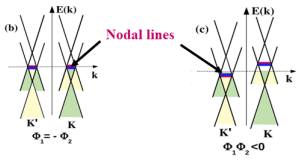

System is gapped by the interlayer hopping which lifts the degeneracy of the nodal lines and opens a gap

Modified Haldane model in AB bilayer: Chern number

For $t_2 \ll t_\perp$: Two-band effective Hamiltonian

$$H_{\text{eff}} = -\frac{\hbar^2 v^2}{t_\perp^2}\left(q_x^2 - q_y^2\right)\sigma_x + 2\xi\frac{\hbar^2 v^2}{t_\perp}q_x q_y\sigma_y + \left(\frac{1}{2}\left(M_1 + M_2\right) - 3\sqrt{3}t_2\xi\right)\sigma_z + \frac{1}{2}\left(M_2 - M_1\right)\sigma_0$$

Quadratic contact point of the AB bilayer graphene + Mass term $m_\xi = \frac{1}{2}\left(M_1 + M_2\right) - 3\sqrt{3}t_2\xi$.

Chern number

$$C = \sum_\xi \chi\frac{1}{2}sgn\left(m_\xi\right) = \pm 2$$

$\chi = -2\xi$ is the valley index of the quadratic point, $\xi = \pm 1$ is the valley index.

AB stacking of two semi-metals with opposite signs of the complex phases becomes a Chern insulator under the interlayer coupling → Stacking-induced Chern insulator

AB bilayer mHM: results

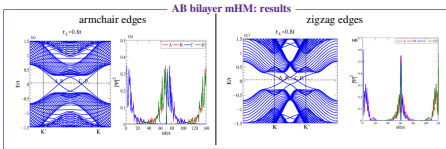

Conclusions

	Uncoupled layers $t_\perp$=0	Coupled layers $t_\perp \neq 0$	Stacking
HM $\Phi_1 = \Phi_2$	$C_1 = \pm 1$, $C_2 = \pm 1$ — Gapped chiral layers	$C = \pm 2$ — Gapped chiral system	AA or AB
HM $\Phi_1 = -\Phi_2$	$C_1 = \pm 1$, $C_2 = \mp 1$ — Gapped chiral layers	$C = 0$ — Gapped trivial system	AA or AB
mHM $\Phi_1 = \Phi_2$	$C_1 = 0$, $C_2 = 0$ — Gapless antichiral layers	$C = 0$ — Gapless antichiral system	AA or AB
mHM $\Phi_1 = -\Phi_2$	$C_1 = 0$, $C_2 = 0$ — Gapless antichiral layers	Gapped trivial system or semi-metal $C = 0$; $C = 0$ — Gapless antichiral system	AA
		$C = \pm 2$ — Gapped chiral system	AB

mm12971@nyu.edu

THE JOURNAL OF PHYSICAL CHEMISTRY C
A JOURNAL OF THE AMERICAN CHEMICAL SOCIETY

pubs.acs.org/JPCC

Article

First-Principles Study of Hydrogen Dynamics in Monoclinic TiO

S. Vahid Hosseini, Andrei Postnikov,* and Mohammad Reza Mohammadizadeh

Cite This: *J. Phys. Chem. C* 2023, 127, 11787−11800

Read Online

ACCESS | Metrics & More | Article Recommendations

ABSTRACT: The existence of intrinsic vacancies in cubic (monoclinic) TiO suggests opportunity for hydrogen absorption, which was addressed in recent experiments. In the present work, based on first-principles calculations, the preferences are studied for the hydrogen absorption sites and diffusion paths between them. The oxygen vacancies are found to be the primary hydrogen traps with absorption energy of −2.87 eV. The plausible channels for hydrogen diffusion between adjacent vacancy sites (ordered in the monoclinic TiO structure) are compared with the help of calculations using the nudge elastic band method. Several competitive channels are identified, with barrier heights varying from 2.87 to 3.71 eV, that are high enough to ensure relative stability of trapped hydrogen atoms at oxygen vacancy sites. Moreover, the possibility of adsorption of molecular hydrogen was tested and found improbable, in the sense that the H_2 molecules penetrating the TiO crystal are easily dissociated (and released atoms tend to proceed toward oxygen vacancy sites). These results suggest that hydrogen may persist in oxygen vacancy sites up to high enough temperatures.

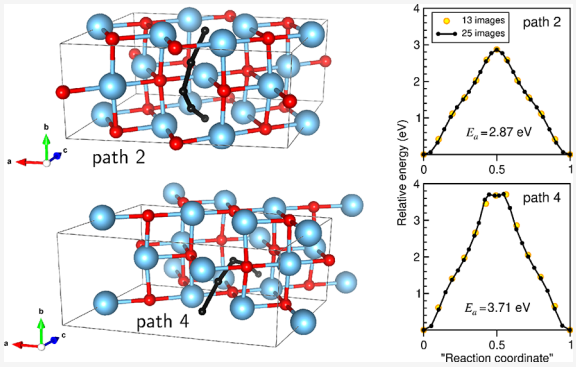

1. INTRODUCTION

The present work aims at elucidating hydrogen trapping and mobility in titanium monoxide. This subject falls within a relatively small intersection of vast domains of research. The hydrogen absorption, storage, and processing in materials is a tremendous and rapidly evolving field; a recent review by Abe et al.[1] may serve as a nice introduction into the subject. Transition-metal oxides are omnipresent in materials science through their different manifestations, over which a concise review by Goodenough[2] offers an efficient guideline. In regards specifically to the hydrogen problematics, transition-metal oxides typically appear as elements of surface protection of metals or as catalytic agents, e.g., in a promising research field of water splitting on oxide-based electrocatalysis,[3] explained, e.g., in recent reviews by Zhu et al.,[4] Song et al.,[5] and Shang et al.[6] Burke et al.[7] summarized the trends in the activity of different transition-metal oxides as catalysts for the *oxygen evolution reaction*. The phenomenon of *hydrogen spillover* came into discussion, in which molecular hydrogen dissociates at the metal surface, and protons diffuse into the catalytic oxide support—see, e.g., ref 8 concerning the process on MgO, or ref 9 for the reaction on VO_2. Whittingham[10] described hydrogen motion in metal oxides; Nolan and Browne[11] overviewed chemical reactions relevant in oxides in relation with hydrogen energy problematics.

Still narrowing the subject, the works from this category dealing with titanium are not numerous and, predominantly, concern the dioxide. Oelerich et al.[12,13] studied the catalytic activity of 3d metal oxides, including TiO_2, and concluded that a tiny addition of them noticeably enhanced hydrogen sorption kinetics of nanocrystalline magnesium. Yin et al.[14] studied, in an experiment supported by first-principles calculations, the adsorption of hydrogen on the surface of TiO_2 with possible diffusion into the depth. Feng et al.[15] looked into the effect of oxygen vacancies in TiO_2 on the enhancing of electrocatalytic activity for *hydrogen evolution reaction* (HER). Oxygen vacancies also play an important role in shaping the *oxygen evolution reaction* essential for water splitting. A recent review on these issues by Zhu et al.[16] covers, among a long list of oxides studied, works on titanium dioxide and oxide-nitride. Hu et al.[17] praised micro- and mesoporous Ti oxides as "in many ways ideal candidates for hydrogen storage because they can be made from inexpensive and light metal Ti, and the surface area, pore size, and wall thickness can be systematically controlled". Li et al.[18] studied the hydrogen evolution activity in epitaxially grown Ti_2O_3 polymorphs.

Titanium monoxide enters the picture as Swaminathan et al.[19] reported that strongly reduced titania (with nominal composition $TiO_{1.23}$, the crystal structure of which reveals X-ray diffraction peaks of disordered TiO) exhibits enhanced HER activity. Recently, Skripov et al.[20] investigated hydrogen

Received: February 2, 2023
Revised: May 26, 2023
Published: June 16, 2023

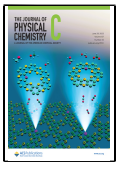

https://doi.org/10.1021/acs.jpcc.3c00750
J. Phys. Chem. C 2023, 127, 11787−11800

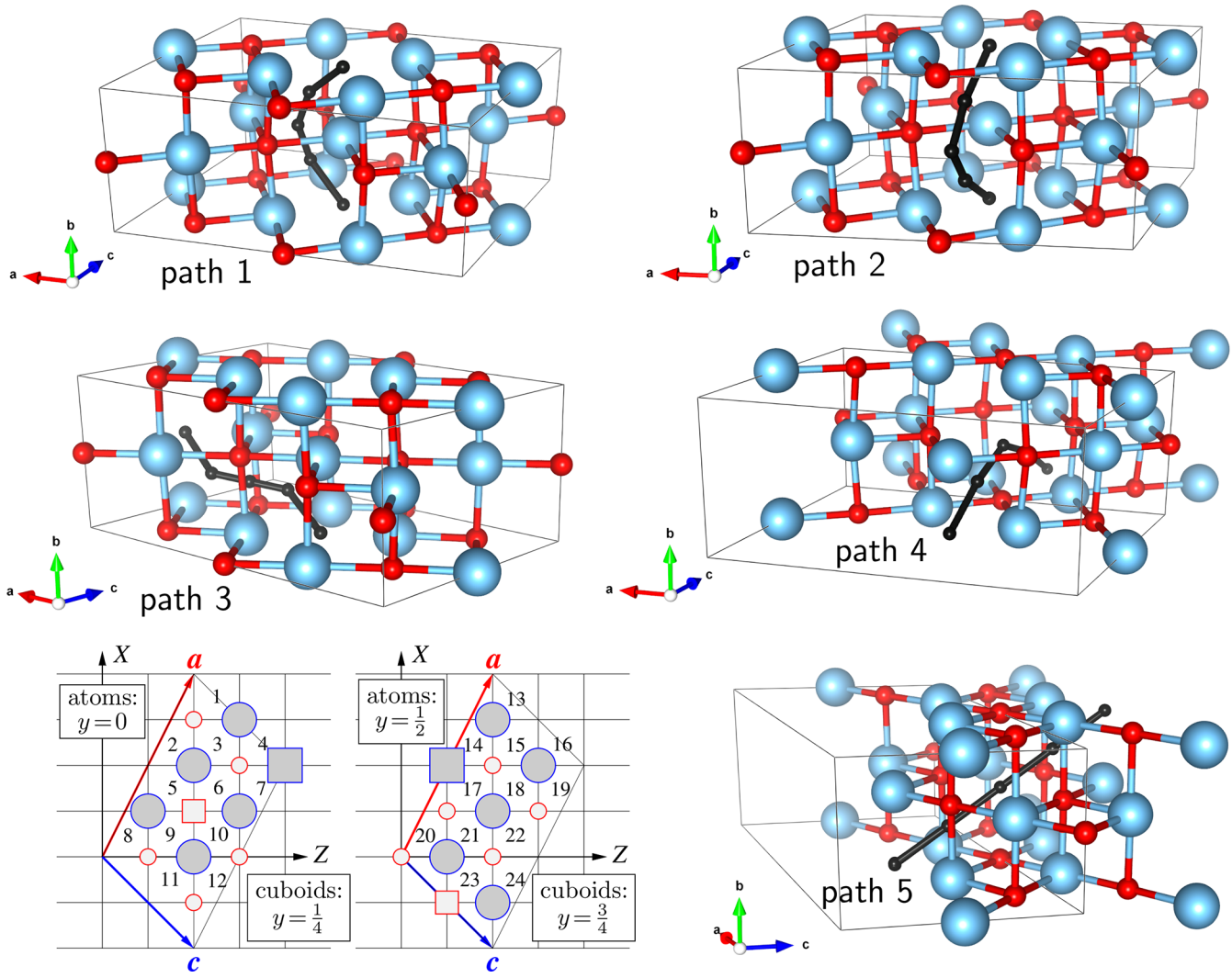

Figure 1. Crystal structure of monoclinic TiO, in side views (Ti atoms shown large blue and O atoms small red), with five different paths (shown in black color as connected intermediate positions) between adjacent oxygen vacancy sites, and (two panels in the bottom left) as two consecutive (010) planes, with atoms shown as circles and vacancy sites shown as squares. The cuboids (centered $y = \frac{1}{4}$ and $y = \frac{3}{4}$) between consecutive atomic layers are numbered, for reference in the text.

absorption in substoichiometric TiO ($TiO_{0.72}H_{0.30}$ and $TiO_{0.96}H_{0.14}$) by a combined use of X-ray and neutron diffraction, neutron vibrational spectroscopy, and nuclear magnetic resonance. This work led to the following conclusions: (*i*) in both nearly stoichiometric and strongly substoichiometric (oxygen-deficient) samples, hydrogen atoms resided exclusively at O vacancy sites; (*ii*) the hydrogenation of nearly stoichiometric, originally B1 disordered, phase provokes an emergence of an ordered (Ti_5O_5 monoclinic) phase coexisting with the disordered (B1-structure) TiO; (*iii*) hydrogen diffusion seems to be insignificant; (*iv*) vibrations of hydrogen atoms occur throughout a broad range of frequencies, presumably as a manifestation of different environments (a possible symmetry-lowering off-center displacement of the trapped hydrogen; a completeness or not of its coordinating Ti octahedron) occurring at different O vacancy sites.

TiO can be crystallized in a cubic B1 (NaCl-type) structure, allowing broad limits of deviation from stoichiometry in the nominal formula TiO_x, namely (citing Watanabe et al.[21]) $0.9 \leq x \leq 1.25$ at 990 °C and $0.7 \leq x \leq 1.25$ at 1400 °C. As mentioned further in ref 21, even in an equiatomic compound about 15% of both titanium and oxygen sites are vacant. The vacancies are randomly distributed at high temperatures; however, on rapid cooling from 1400 to 990 °C, they get ordered, resulting in a monoclinic phase, which is in fact the underlying B1 with 1/6 of sites on each sublattice being vacant. While deficiency on either cation or anion sublattice is not uncommon in materials, the coexistence of vacancies in both sublattices is relatively rare and, among the metal monoxides, is known to occur only in TiO,[22,23] VO,[24] and NbO.[25]

Theoretical studies of TiO have a long history. Neckel et al.[26] performed a self-consistent electronic structure calculation of TiO (among other transition-metal oxides and nitrides with B1 structure, assumed perfect and complete). This revealed the essential in the placement and composition of different energy bands. Leung et al.[27] compared the relative stability under pressure of several Ti- and O-deficient (stoichiometric) ordered phases, including the "true" monoclinic Ti_5O_5 and several more symmetric ordered-vacancies phases; the energy preference of the monoclinic phase has been demonstrated. Andersson et al.[28] offered a more detailed analysis of different

https://doi.org/10.1021/acs.jpcc.3c00750
J. Phys. Chem. C 2023, 127, 11787−11800

vacancy-ordered phases, in comparison with a model of disordered alloy (of vacancies) on each sublattice. (One can add in this relation that a much earlier attempt of a "vacancy-alloying" approach to the electronic structure of TiO, non self-consistent and within virtual crystal approximation, was undertaken by Schoen and Denker.[29]) Graciani et al.[30] in an almost simultaneous work reiterated the established reasons for the structural preference of the monoclinic phase. Kostenko et al.[31] concentrated on comparing the ordered monoclinic Ti_5O_5 phase against the B1 vacancy-disordered one, whereby the latter was simulated by averaging the results over 20 different supercells of (40 × Ti+40 × O) atoms (plus 8 × Ti+8 × O vacancy sites). Under this perspective, we considered the monoclinic TiO phase to be a perfect model system—not too simplistic yet well-defined—for studying hydrogen trapping, vibration, and diffusion. A different choice, that of disordered B1 lattice, would make the results too much dependent on the particular model(s) of disorder used. An ambition of the present work is to challenge the conclusions formulated by Skripov et al.,[20] on the basis of first-principles calculations, and/or to give these qualitative conclusions a numerical expression. Specifically, we probe adsorption energies of hydrogen at different sites, calculate vibration modes of the crystal doped with hydrogen, identify plausible diffusion paths, and estimate corresponding energy barriers.

In its concept, our work has certain similarities with an *ab initio* simulation by Kajita et al.[32] done for hydrogen adsorption at the TiO_2 surface, in the sense that different trapping sites have been identified, and the energy barriers between them explored. The difference is in the crystal structure of the underlying oxide and in that we considered a 3-dimensional crystal in our simulation and not a surface represented by a slab.

The present work is organized as follows. Section 2 explains the crystal structure, adsorption sites, and the paths between them. Section 3 outlines technical details of first-principles calculations. Section 4 presents the results of hydrogen binding energy and intersite barriers, with its impact on diffusion. The conclusions are summarized in section 5.

2. CRYSTAL STRUCTURE AND GEOMETRY OF VACANCIES

The stable monoclinic structure of nominally stoichiometric TiO (which holds however in the concentration range $TiO_{0.7}$ through $TiO_{1.25}$) has been identified by Watanabe et al.[21,33] In terms of the lattice parameter of the nominal underlying cubic (B1) lattice, and in the setting to be used in the following, the monoclinic lattice comes about spanned by $\mathbf{a} = [2\ 0\ 1]$, $\mathbf{b} = [0\ 1\ 0]$, and $\mathbf{c} = [\bar{1}\ \ 0\ \ 1]$ vectors. Correspondingly, the unit cell contains 3 × 4 = 12 of both anionic and cationic sites, of which only 10 (of each species) are occupied. Further on, $a/b = \sqrt{5}$, $c/b = \sqrt{2}$, and $\beta = \pi - \arctan(3) = 108°26'$. These relations, as we will see, are slightly modified due to the presence of vacancies. The distribution of vacancies centers the (a, b) face (space group $C2/m$, unique axis b); hence, the primitive cell in fact includes five Ti and five O atoms. Their arrangement over Wyckoff positions with coordinates refined in experiment can be found in ref 21. The unit cell, in several side views (with different diffusion paths, see below) and as a [010] projection of two consecutive atomic planes $y = 0$ and $y = \frac{1}{2}$, is shown in Figure 1. The choice of the unit cell is such that Ti vacancy is at the origin. These projection figures specify, for further reference, the numbering of Ti_4O_4 cuboids (eventually with vacancies, represented by squares instead of circles, at some vertices) centered in the $y = \frac{1}{4}$ and $y = \frac{3}{4}$ planes.

A priori, the possible hydrogen absorption sites are expected to possess certain symmetry; plausible candidates are interstitial positions (inside the Ti_4O_4 cuboids, probably with one or two corner atoms missing), the Ti vacancy sites, or the O vacancy sites. All these possibilities have been explored (see the details below), with the conclusion that the oxygen vacancies are the ground-state configurations, Ti vacancies are metastable local minima, and the other trial configurations end up squeezed out into one or the other of the two mentioned. Anticipating the question of hydrogen diffusion between the oxygen vacancy sites, we can already elaborate on the possible trajectories connecting such adjacent positions. Figure 1 summarizes all possible paths connecting adjacent O vacancies, shown as straight-line fragments through the centers of different (numbered) cuboids. In practical calculations using the Nudged Elastic Band (NEB, see below) technique, the trajectories will be shortened/smoothened.

Making reference to numbered cuboids (at the bottom left of Figure 1) which "pave" two alternating (010) planes of the monoclinic structure, the paths under discussion can be identified as follows.

Both path 1 and path 2 connect the O vacancy sites separated by [0 1 0] move, circumventing the Ti atom in between. The path 1 goes ("upwards", from the O vacancy position with $y = 0$) through cuboids 6 and 18 (or, equivalently, 9 and 21); the barrier is obviously anticipated on squeezing through the Ti_2O_2 face in between. The path 2 goes through cuboids 5 and 17 (or, equivalently, 10 and 22). The saddle point at $y = \frac{1}{2}$ occurs now on squeezing through a face which is not complete, because the cuboids in question share a titanium vacancy. Consequently, the path is expected to be pushed either toward or away from this vacancy, and the barrier to become lower than for path 1.

A "watershed" between the paths 1 and 2, with their corresponding saddle points, would be on the Ti−O bond, breaking which is likely to cost much energy.

Path 3 is a $\left[\frac{1}{2}\ \ \frac{1}{2}\ \ 0\right]$ diagonal move, through the cuboids 6 and 3 (or, equivalently, 9 and 11); the bottleneck is squeezing through a complete Ti_2O_2 face underway. Consequently, the barrier is expected to be similar to that on path 1.

Path 4 goes in general [0 0 1] direction, making a bow around the O atom situated halfway, through the cuboids 10 and 5 (or, equivalently, through the cuboids 22 and 17 under the $y = 0$ plane). This path is likely to go through (or, rather, just close to) the Ti vacancy site (at $y = \frac{1}{2}$) shared by the two cuboids in question. In this sense, the path 4 resembles path 2; the difference is that an oxygen and not titanium atom is circumvented.

Path 5 goes straight along [0 1 1] through, e.g., the cuboids 10 and 17, via the Ti vacancy site situated halfway (in the corner shared by the both cuboids). We note in this relation that passing *exactly* through the Ti vacancy on this path is imposed by symmetry (that was not the case of paths 2 and 4); therefore, the barrier height must match the difference of hydrogen absorption energies in the Ti and the O vacancies. We will come back to this point in discussing the results below.

https://doi.org/10.1021/acs.jpcc.3c00750
J. Phys. Chem. C 2023, 127, 11787−11800

In practical calculation of hydrogen absorption energies and diffusion, we were careful to use sufficiently large supercells so that the hydrogen atom could be treated as an isolated impurity, and the effects of spurious periodicity within the hydrogen "sublattice" could be minimized.

3. COMPUTATIONAL DETAILS

Electronic total energies and forces (for conjugated-gradient structure relaxation and the extraction of force constants) were calculated within the density functional theory (DFT), using the generalized gradient approximation (GGA) for exchange-correlation functional in the flavor of Perdew−Burke−Ernzerhof (PBE).[34]

Whereas in many calculations done for TiO_2 and Ti_2O_3, the inclusion of correlation effects beyond the conventional GGA was considered necessary and was treated within "GGA+*U*" scheme or using hybrid functionals (see, e.g., Hu and Metiu[35] for a review), no such need seems to apply to metallic titanium monoxide.

A large part of our calculations have been done with the help of the Quantum ESPRESSO (QE) package,[36,37] using plane waves as basis functions, and otherwise, so that some results would have been cross-checked, with the SIESTA code,[38,39] which relies on atom-centered localized basis functions. The ultrasoft pseudopotentials[40] were employed in QE calculations, whereby Ti 3s, 3p, 3d, 4s, O 2s, 2p, and H 1s states were included as valence ones. In SIESTA calculations, norm-conserving pseudopotentials[41] were used, with the attribution of valence states as indicated above, except for the Ti 3s states, which were treated as core. The idea of using two methods evolved naturally from a need to apply adequate tools to different tasks but eventually offered an opportunity to compare parallel predictions as well, which turned out to be helpful in assessment of credibility of numerical results. In fact, even if two codes operate at the same level of theory (DFT/GGA), details of technical implementation may be responsible for slightly different numerical results. Whereas some parameters (**k**-mesh, plane-wave cutoffs) can be systematically enhanced to yield necessary precision, the others remain somehow an experience-guided free choice. Such is the generation of pseudopotentials, not identical in two methods, and a construction of basis functions in SIESTA. Whereas QE is robust and free from ambiguity with regard to the choice of bases, SIESTA with its compact yet efficient basis sets might be interesting for trading its applicability to very large systems for an affordable loss in accuracy. In our present compromise, we place on QE our expectations of, a priori, higher accuracy, recognizing at the same time that the size of systems treated with QE risks to be not sufficiently large for making a good model case of isolated impurity. If the methods used are, in a sense, complementary, their combination may help to reasonably estimate the error margin due to inherent technical differences and to judge about the general credibility of results.

In QE calculations we used $1 \times 2 \times 2$ supercells (40 TiO formula units), and in SIESTA calculations $-1 \times 3 \times 2$ ones (60 TiO formula units), which helped to ensure a more even separation between impurities on the lattice. The **k**-mesh used for summations over the Brillouin zone according to the Monkhorst−Pack scheme[42] was more dense in the second case ($6 \times 5 \times 5$ divisions along the reciprocal lattice vectors) than in the first one ($4 \times 4 \times 4$ mesh points). The planewave cutoff for the basis set construction in QE was set to 60 Ry; the cutoff for kinetic energy and charge density expansion was set to 720 Ry. The MeshCutoff parameter for the expansions of residual charge density in SIESTA was set to 300 Ry. The convergence for energy was chosen as 10^{-5} eV between two ionic steps, and the maximum force allowed on each atom is 0.01 eV/Å. Comparing with earlier works, we can state that our QE calculation setup is closest to that used by Kostenko et al.[31] in regard to the code applied, the exchange-correlation potential, and the supercell size. The differences are that there was no extrinsic impurities considered in ref 31, nor optimization done for lattice parameters (of supercells simulating disorder). Therefore, we can address the reader to Figure 7b of ref 31 for inspecting the local densities of states (DOS) in the ordered phase, which exhibit a characteristic pseudogap at the Fermi level, discussed in some of the works cited. Partial DOS in the presence of hydrogen impurity, obtained with SIESTA, will be shown and discussed below. Incorporation energy of a hydrogen atom at a vacancy site is expressed as

$$E_{\mathrm{H}}^{I} = E_{\mathrm{TiO+H}} - E_{\mathrm{TiO}} - E_{\mathrm{H}} \quad (1)$$

where $E_{\mathrm{TiO+H}}$ is the total energy of TiO supercell containing a H atom, E_{TiO} is the total energy of pristine TiO supercell, and E_{H} is the energy of isolated H atom. Applying such a formula to total energy results obtained with SIESTA (or, with any other method employing atom-centered basis functions) demands to correct for basis set superposition error (BSSE, see ref 43). In practical terms of our case, this involved placing hydrogen basis sets ("ghost atoms" not carrying core charges nor electrons) at two relevant (trial) positions for hydrogen adsorption. Either one (for calculating $E_{\mathrm{TiO+H}}$) or none (for E_{TiO}) of these positions were in fact occupied by hydrogen atom, the rest being ghosts. Correspondingly, E_{H} stems from a calculation for the same supercell of the same shape, in which a single (spin-polarized) genuine hydrogen atom cohabits with 121 ghosts.

Inspection of minimum energy paths (MEPs) connecting distinct local minima (typically over a saddle point) can be, from the side of theory, conveniently done by the Nudged Elastic Band (NEB) method, implemented in the QE code. Reference 44 offers an overview of NEB and other related schemes, which deal with a sequence of intermediate "images", e.g., conformations of the system subject to interplay of forces "along" and "away from" the path, ensuring the smoothness and the shortness of the latter. In the present calculations, we considered 13 images and (independently) 25 images, in order to check the stability of results against this parameter; k_*min* and k_*max* switches for elastic bands were chosen at 0.2 and 0.3 Ha, respectively.

4. RESULTS AND DISCUSSION

Our calculations included unconstrained structure relaxation of (for reference purposes) pristine monoclinic TiO and, in appropriately enlarged supercell, of hydrogen impurity tentatively placed in various lattice positions. It turned out that the hydrogen remains (the most) stable at an oxygen vacancy site but also at a local energy minimum at a titanium vacancy site. Hydrogen escapes from other symmetric positions, e.g., in the centrum of a Ti_2O_2 face or cutting a Ti−O bond.

4.1. Equilibrium Crystal Structures; Comparison of Methods. Some results reported below (lattice relaxations, energy barriers) have been obtained with two methods, QE and SIESTA. Even if QE, free from ambiguities in constructing the basis functions, might be considered as ultimately more

https://doi.org/10.1021/acs.jpcc.3c00750
J. Phys. Chem. C 2023, 127, 11787−11800

Table 1. Sizes of Empty or H-Occupied Octahedral Cages, According to GGA Calculations. For Comparison, Lattice Parameters Mapped onto a Single Monoclinic Cell Are Given. See Text for Details

	dimensions (Ti−Ti in Å) of $\square_O$ along...			dimensions (O−O in Å) of $\square_{Ti}$ along...			reduced lattice parameters (Å)[a]		
System	$[10\bar{1}]$	[102]	[010]	$[10\bar{1}]$	[102]	[010]	*a*	*b*	*c*
Quantum ESPRESSO calculations (1 × 2 × 2 supercells)									
pristine	3.905	4.102	4.163	4.247	4.328	4.163	9.319	4.163	5.845
H@$\square_O$	3.945	4.098	4.110	4.241	4.316	4.162	9.330	4.162	5.839
H@$\square_{Ti}$	3.889	4.091	4.171	4.337	4.404	4.309	9.329	4.165	5.853
SIESTA calculations (1 × 3 × 2 supercells)									
pristine	3.926	4.239	4.226	4.340	4.489	4.247	9.507	4.224	5.954
H@$\square_O$	3.997	4.242	4.185	4.321	4.479	4.252	9.510	4.229	5.958
H@$\square_{Ti}$	3.921	4.241	4.230	4.398	4.535	4.362	9.511	4.224	5.953
X-ray diffraction by Watanabe et al.[b]									
pristine	4.026	4.197	4.142	4.233	4.256	4.142	9.340	4.142	5.855

[a]Crystallographic angle was within +0.06% in QE calculations and within −0.5% in SIESTA calculations from the experimental value $\beta = 107°32'$ as reported in ref 21. [b]Ref 21; the original attribution of crystallographic parameters is changed in the table to match that in later works.

reliable (for the given supercell geometry and similar pseudopotentials), we prefer to expose the SIESTA results along with those by QE. This will help to get some idea of the "credibility margin", in view of SIESTA being applied to larger-size supercells and yielding some supplementary properties to those explored by QE.

Table 1 shows the structure parameters of nominal (pristine) TiO, in comparison with experiment, and the (predicted) modification of structure under insertion of hydrogen. SIESTA tends to overestimate the lattice parameters (by at most 2% against the results by Watanabe et al.;[21] by ≃5% for the volume), whereas QE seems to perform much better, within 1% of experiment values for every lattice parameter and the volume. However, the dimensions of cages around oxygen vacancies are estimated with SIESTA at least not worse than with QE (judging again by comparison with experiment). What seems important for the following is that the distortion of vacancy cages (measured between two opposite atoms flanking either the vacancy, or the hydrogen atom occupying the vacancy site) upon insertion of hydrogen follows the same pattern according to either QE or SIESTA and seems reliable beyond the calculation "noise": a roughly uniform expansion (by 1−2%) occurs around hydrogen occupying the Ti vacancy, whereas around hydrogen at the O vacancy site, an expansion along the long diagonal of the unit cell (i.e., parallel to $[10\bar{1}]$) is combined with compression in the perpendicular direction ([102]). In Table 1, those distances which noticeably (by ≃1%) shrink as compared to the situation in a pristine lattice are overlined in the table; those which expanded (by at least the same margin) are underlined. The average lattice parameters (shown in the three last columns of Table 1) and the dimensions of the hydrogen-free vacancy cages remain practically unchanged.

4.2. Adsorption Energies, Lattice Relaxation, Electronic Structure. Hydrogen incorporation energies calculated according to Eq. 1 yield, with total energies from QE calculations, −2.87 eV at the O vacancy site (hence energetically favorable insertion) and +0.75 eV at the Ti vacancy site (hence costing energy). Even if straightforwardly identifiable from the point of view of calculation, these values might be not so easy to relate to experiment, because of ambiguity and difficult reproducibility of reference situations, e.g., molecular hydrogen penetrating the crystal, dissociating, etc. "Straightforward" SIESTA calculations, performed without correcting for BSSE, are in qualitative agreement with QE results, yielding −3.13 and +0.20 eV for adsorption at the O vacancy and the Ti vacancy sites, respectively. SIESTA calculations staged to minimize the systematic error by excluding the BSSE, e.g., done with the equal number and positions of (either real or ghost) atoms in the three situations relevant for Eq. 1, result in adsorption energies of −2.86 eV (H@$\square_O$) and +0.73 eV (H@$\square_{Ti}$). Such good agreement between results of planewave-basis and localized-basis methods, even if ideally anticipated, is not always secured technically and can serve here as an additional argument for the credibility of results.

The variations of total energies have their origin in the fine details of the electronic structure, even if the direct relation might be difficult to trace. Figure 2 depicts local densities of states at the hydrogen atom at the O vacancy, its nearest Ti neighbors, and both these species averaged over the supercell.

An inspection of Mulliken populations done with the SIESTA code (comparing the fully relaxed situation of a hydrogen insertion with the pristine crystal and ghost atom at the vacancy site) shows an inflow of about 0.1 electrons onto H at the O vacancy site from its surrounding Ti atoms. Interestingly, a certain analogy can be found between this system and the rocksalt TiH hydride, addressed in a number of first-principles simulations:[45,46] the placement of H-related band at ≃6−8 eV below the Fermi level, the charge transfer toward H, the general shape and energy placement of the Ti 3d band, the order of magnitude of the formation energy. Especially Smithson et al.[46] paid attention to elucidating different contributions to the hydride formation energy, including conversion of the metal structure to face-centered cubic (fcc), expansion to the optimal lattice parameter, and chemical bonding to hydrogen. Under this angle, a H-occupied O vacancy in titanium monoxide is already in a "favorable" fcc (rocksalt)-like environment of Ti atoms, whereby the distances between the latter (cf. Ti−Ti size of the O vacancy cage in Table 1) roughly match the lattice parameter of the rocksalt titanium hydride (4.10 Å, according to Table 2 of ref 46). A discussion around Figure 6 in the same work specifies the details of charge loss by Ti e_g orbitals in favor of H-centered spherical distribution. Much of this discourse applies to our system as well. Focusing on the details specific for H at the O vacancy in TiO, we note that the Ti DOS is characterized by a dip at the position of the Fermi level, marked in earlier

https://doi.org/10.1021/acs.jpcc.3c00750
J. Phys. Chem. C 2023, 127, 11787−11800

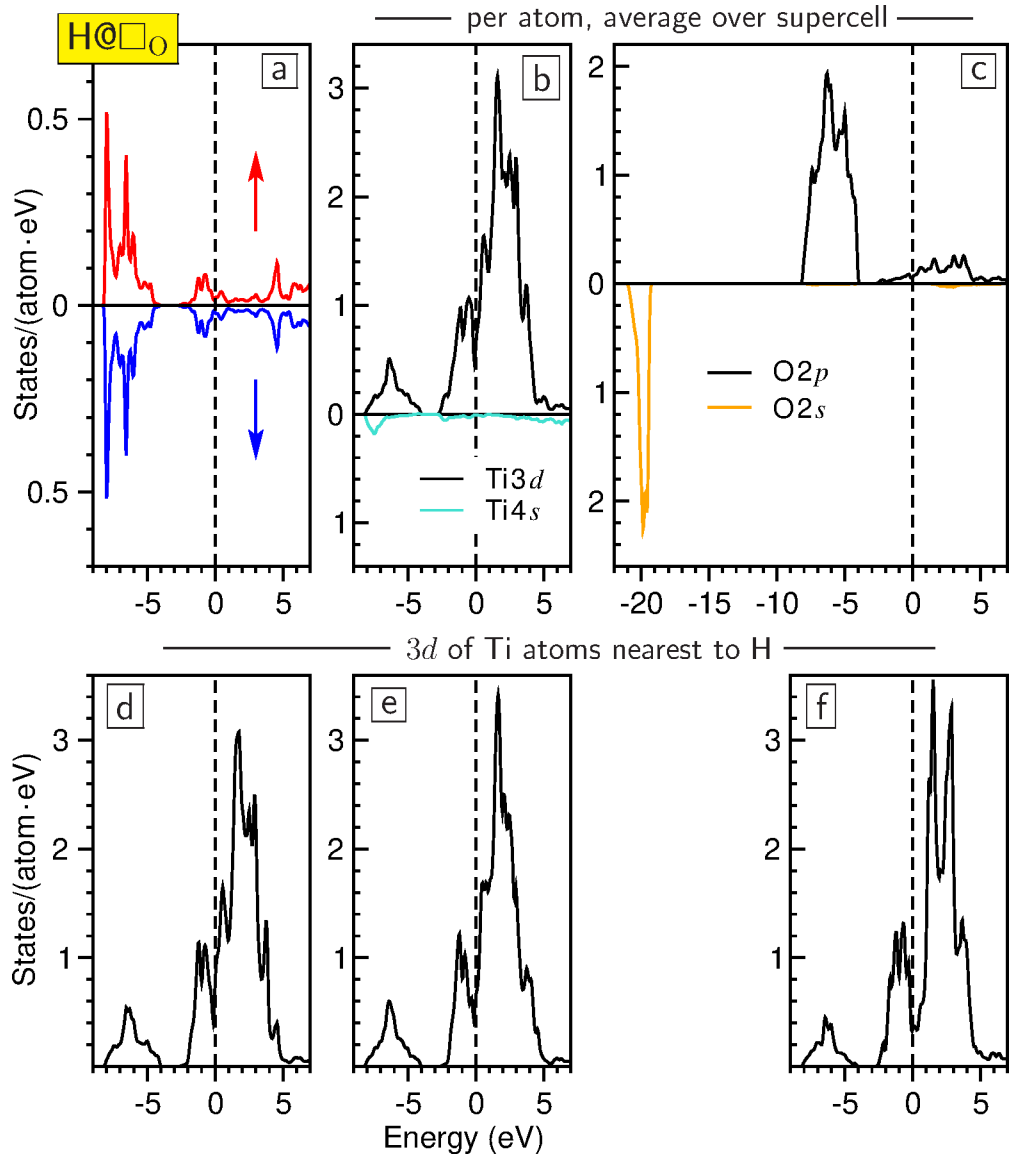

Figure 2. Partial densities of states (DOS) in relaxed 1 × 3 × 2 (120 atoms) supercell of monoclinic TiO, containing also a hydrogen atom at the oxygen vacancy site, from a SIESTA calculation. Zero energy (dashed vertical line) corresponds to the Fermi energy. The upper row includes (a) spin-resolved DOS of H atom (in fact nonmagnetic in this position); (b) 3d and 4s DOS of Ti (averaged over all Ti sites in the supercell); (c) 2s and 2p DOS of O (averaged over all O sites in the supercell). The bottom row depicts the 3d DOS for three symmetrically distinct pairs of Ti atoms octahedrally bordering the vacancy site occupied by hydrogen, namely, atoms situated at (d) $\pm\frac{1}{6}(\mathbf{a}-\mathbf{c})$, (e) $\pm\frac{1}{6}(\mathbf{a}+2\mathbf{c})$, and (f) $\pm\frac{1}{2}\mathbf{b}$, in units of nominal translation vectors of the monoclinic structure (cf. Figure 1).

calculations of monoclinic TiO.[27,47] Among the six Ti atoms neighboring the inserted hydrogen, the two closest to it (compacted toward hydrogen along [010], see Table 1) develop the most pronounced difference (two distinct peaks just above the Fermi level, see Figure 2f) from the pristine (or, lattice-averaged, cf. Figure 2b) Ti DOS.

The other possible placement of H in TiO, at the Ti vacancy site, is a metastable one, with elevated total energy yet corresponding to a local energy minimum. The peculiarity of this configuration is the local magnetic moment of 1 μ_B inherited from a free hydrogen atom, due to a relative absence of chemical bonding and of charge transfer in either direction between H and its surrounding oxygen atoms. We will see in the following that the stability of the magnetic solution is rather sensitive to an off-center displacement of hydrogen. Figure 3 shows the spatial distribution of the spin density which is strongly localized on the impurity, yet slightly spills out onto the neighboring O atoms, especially onto those at $\pm\frac{1}{2}\mathbf{b}$. This observation is further reinforced by an inspection of partial DOS concerning H at the Ti site and its neighbors (Figure 4). The most remarkable feature of the magnetic structure is a narrow majority-spin state just below (by $\simeq$1 eV) the Fermi level. This state, strongly localized at hydrogen, also manifests itself in the partial DOS of O neighbors, primarily those along [010]—cf. Figure 4f. The spatially resolved density of electronic states, integrated in energy just over this peak (done with SIESTA, not shown here) closely reproduces the full spin density revealed by Figure 3.

Despite the practical absence of the charge transfer, the electronic shells of oxygen atoms are spin polarized to (together over the six atoms) 0.12 μ_B. This polarization is

https://doi.org/10.1021/acs.jpcc.3c00750
J. Phys. Chem. C 2023, 127, 11787−11800

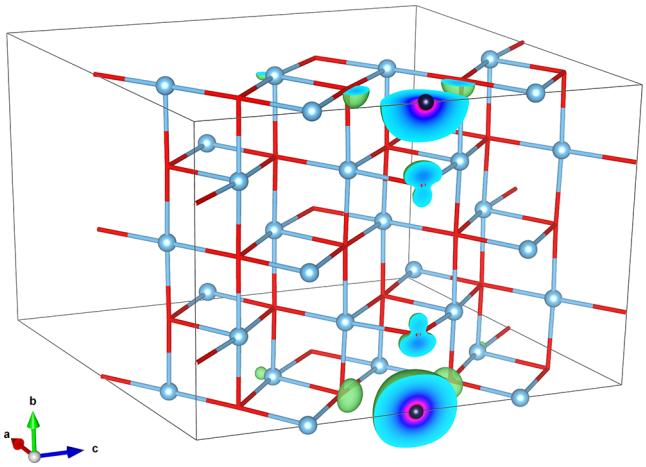

Figure 3. Spin density map calculated with QE for the supercell with hydrogen (small black sphere) at the Ti vacancy site. Ti atoms are marked by blue spheres; O atoms are marked by red crosses in the wireframe. The isosurface shown in green corresponds to the level of 0.003 μ_B Å^{-3}; the color schema in the cuts by the unit cell faces means enhancement from cyan to magenta. As the isolevel increases, the surfaces rapidly become spherical and compact around the H site. In total, there is 1 μ_B per H atom.

two times stronger on the "out-of-plane" atoms [situated at $\pm\frac{1}{2}$**b**, marked (f)] in Figure 4 than on the "in-plane" atoms, marked (d) and (e), as is also revealed by the manifestation of the features below the Fermi energy in the corresponding partial DOS.

For a more systematic insight into the variance of properties at two possible sites for hydrogen, we show in Figure 5 a simulated smooth transition between them, along the path 5 of Figure 1. Calculated energy profile, the Mulliken charge at the H atom, and the total magnetic moment stem from a row of SIESTA calculations, in which H atom was fixed at the intermediate positions along the path, its nearest neighbors were free to relax, and more distant atoms in the supercell were kept frozen. This can be considered as a forerunner of more general and flexible NEB calculations over the ensemble of paths, to be discussed below. One clearly sees that the relative energy increases along the path, consistently with the energetics discussed above in subsection 4.2, until eventually the magnetic solution sets up, resulting in a modest energy lowering. The "potential well" around the Ti vacancy site is ≈1 Å wide and ≃0.1 eV (or ≃1160 K) deep, so that the zero-point energy for hydrogen in it is about 30 meV; hence, this site seems plausible for hypothetical trapping of hydrogen.

One notes that the magnetic solution sets up abruptly and maintains the value of almost exactly 1 μ_B, even if the system, being metallic, does not impose an integer value of the magnetic moment. This reinforces the hypothesis that hydrogen at a Ti vacancy site behaves as a trapped free atom. Consistently with this view, the Mulliken charge, somehow elevated throughout the "hydride-like" part of the path, drops down to 1.1, a nearly nominal value for a free atom.

The bump in the value of the Mulliken charge at 1/3 of the distance from O-vacancy to Ti-vacancy occurs as the hydrogen atom squeezes between three titanium atoms, across a face of a Ti-octahedron delimiting the O-vacancy cage. This bottleneck is characterized by a charge flow from Ti to H; the total energy curve goes markedly upward from the direct linear slope. At 2/3 of the distance, the hydrogen atom passes through a triangle of oxygen atoms without a noticeable hybridization or charge loss, and, being released into the O-octahedron around the Ti vacancy site, it looses extra charge and recovers its free-atom magnetic moment. A slight rearrangement of states within the occupied fraction of Ti3d−O2p bands accounts for a lowering of total energy. Gradually uprising energies of forced zero-spin solutions (cf. light green dots at the right edge of the upper panel in Figure 5) demonstrate that magnetism of H at the Ti-vacancy site is essential for the (meta)stability of this configuration.

4.3. Phonons. For additional insight, and also in order to offer some discussion of interesting neutron energy loss spectra published by Skripov *et al.*,[20] we calculated the density of vibration modes for H-doped (one atom per supercell) monoclinic TiO. The QE calculation used a density functional perturbation method, and SIESTA − frozen phonon calculation. In both these cases, just Γ phonons for the corresponding supercell have been calculated, yielding 243 and 363 modes, respectively. The resulting densities of modes are depicted in Figure 6, slightly broadened (with halfwidth parameter of 5 cm^{-1}) for better visibility. The above-mentioned neutron scattering spectrum is reproduced for comparison, with energy axes properly aligned.

One notes an encouraging agreement between the Ti/O parts of the vibration spectra obtained by two methods, the degree of such agreement being not a priori obvious in view of a certain difference in calculating the electronic structure and the assessment of phonons. As was correctly anticipated in ref 20, the low-energy (≃60 meV) peak in their neutron scattering spectra (cf. Figures 4 and 5 of the work cited) is due to optical vibrations of oxygen atoms. Moreover, based on inspection of vibration patterns in different modes one can now conclude that the split-off peak at the top of the oxygen vibration band at ≃600 cm^{-1}, which is also pronounced in the experimental spectrum, reveals the vibrations of 4-coordinated oxygen atoms, i.e., those bordering to Ti vacancies at $\pm\frac{1}{2}$**b**.

Hydrogen vibrations make three distinct lines, a close "doublet" at ≃800−900 cm^{-1} and a markedly distant peak at ≃1200 cm^{-1}. This general picture holds for both SIESTA and QE calculations, even if precise frequencies differ (756, 784, 1188 cm^{-1} in SIESTA calculation vs 842, 943, 1250 cm^{-1} according to QE). This picture agrees well with the observation by Skripov et al.[20] that "... the spectra look like superpositions of two broad bands centered at about 115 meV and about 155 meV", taking into consideration a "volatility" of calculated frequencies under the slightest modification of calculation conditions, due to the smallness of the proton mass. A direct inspection of the modes in question reveals that the vibrations occur along the Ti−Ti axes of the Ti_6 octahedron, i.e., [102], [010], and [10$\bar{1}$], respectively. The variance in vibration frequencies nicely correlates with the sizes of Ti_6 cages (cf. Table 1) and the hence following steepness of the potential well confining the hydrogen vibrations. Namely, the softest of the three vibrations occurs along the direction of the largest Ti−Ti distance, that is, [102] according to SIESTA and [010] according to QE. This "contradiction" is not crucial because these two cage dimensions are not much discriminated. On the contrary, the markedly split-off hardest mode represents the vibration along [10$\bar{1}$], the shortest cage size, in both SIESTA and QE calculations.

https://doi.org/10.1021/acs.jpcc.3c00750
J. Phys. Chem. C 2023, 127, 11787−11800

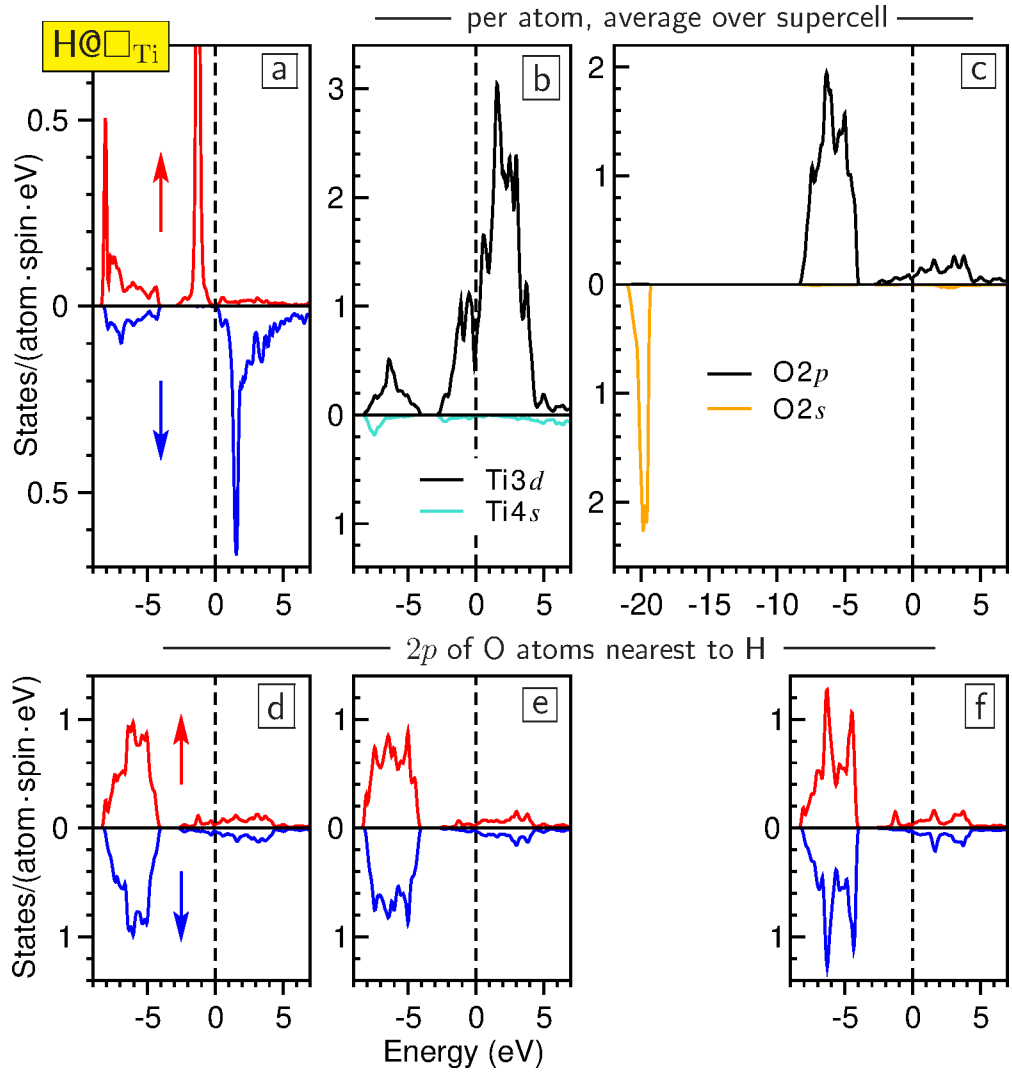

Figure 4. Similar to Figure 2, for the case of a hydrogen atom at the titanium vacancy site. The system possesses the magnetic moment of 1 μ_B. The bottom row depicts 2p DOS of O atoms around the Ti vacancy site, namely, atoms situated at (d) $\pm\frac{1}{6}(\mathbf{a}-\mathbf{c})$, (e) $\pm\frac{1}{6}(\mathbf{a}+2\mathbf{c})$, and (f) $\pm\frac{1}{2}\mathbf{b}$.

Skripov et al.[20] suggest that "... the high-energy band at about 155 meV ... may be ascribed to the characteristic environment of H in the monoclinic phase", to which statement we now offer an adjusting explanation.

It was emphasized in ref 20 that "... the volume of the voids formed by oxygen vacancies is too large for H atoms, so that a hydrogen atom can be easily displaced from the geometrical center of the vacancy" and "... for a considerable number of H atoms, the nearest-neighbor environment is no longer octahedral". In fact we show that off-center displacement is not crucial for explaining broad peaks and that, even when preserving an octahedral environment, slightest modifications of the latter's shape and size due to all possible distant imperfections in the lattice are capable to generate a broad band of hydrogen vibration frequencies, typical for spectra of real materials.

4.4. Dissociation of H_2 Molecule. In the study of hydrogen uptake and diffusion in metals, it is generally accepted that the H_2 molecule is first physisorbed at the surface and may then overcome the activation barrier for dissociation (see, e.g., a discussion around Figure 1 of Kirchheim and Pundt[48]). Hydrogen atoms may further be chemisorbed and eventually diffuse into the material. As in the discussion about hydrogen diffusion (see next subsection), quantum effects may be important in overcoming the activation barrier; an early representative work to this effect, simulating dissociative adsorption (of H_2 on Cu surface), was done by Mills and Jónsson.[49] We do not address this issue here in details, but, as the geometry and the properties of TiO are somehow different from common metals, we wonder whether a hydrogen molecule may fit into, and survive intact within, the oxygen vacancy cage.

As it turns out in the course of conjugate-gradient total energy minimization (see Figure 7, one example out of several trial ones starting from different initial orientations), the molecule eventually "almost dissociates", doubling the nominal H−H bond length to ≃1.4 Å. It looks like every hydrogen atom preferentially "couples" to three closest Ti atoms, in the spirit of the remark made in the previous subsection about the oxygen vacancy cage being too large for a hydrogen atom. We did not manage to reproduce a definite dissociation, when one of the H atoms would flee the Ti_6 cage delimiting an oxygen vacancy site, because this would require an energy inflow to overcome a barrier (see next subsection); however, such an event seems to be within grasp for a molecular dynamical high-temperature simulation. Indeed, an energy step of ≃1.2 eV (see

https://doi.org/10.1021/acs.jpcc.3c00750
J. Phys. Chem. C 2023, 127, 11787−11800

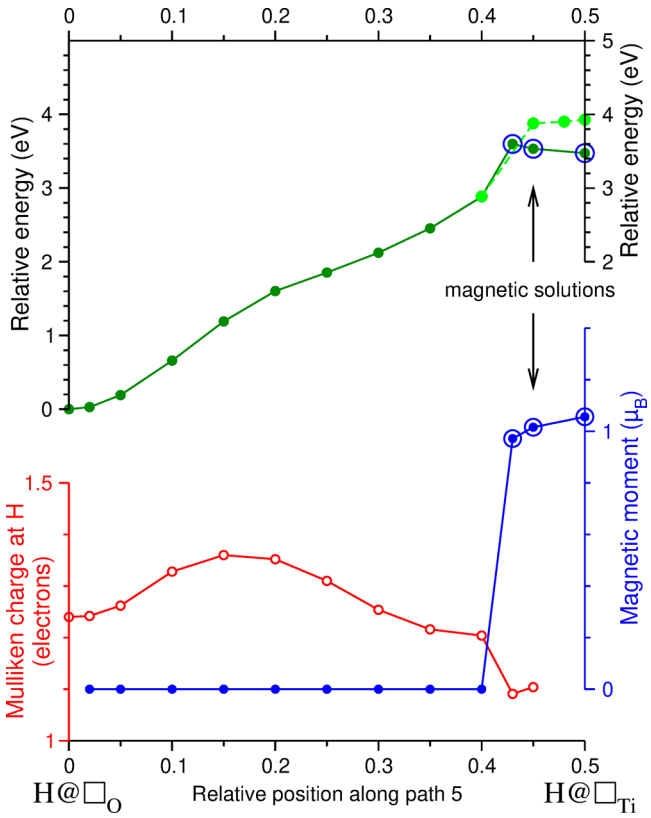

Figure 5. Variation of total energy, magnetic moment, and Mulliken charge at the H atom in the course of the latter's continuous displacement from O-vacancy to Ti-vacancy position (after SIESTA calculations, allowing the relaxation of atoms along the path). Magnetic solutions, which survive only in small vicinity of the Ti vacancy, are marked by circles. The energy values for their nonmagnetic counterparts are indicated by light green dots.

Figure 7) separates the "weakened"/expanded H_2 molecule from a situation when one of its constituent H atoms is promoted out of the crystal. An irrevocable dissociation and diffusion away from the original site of an atom remaining within the crystal may presumably cost less energy.

4.5. Energy Barriers for Hydrogen Atom Hopping over Oxygen Vacancy Sites. We turn now to the discussion of scenarios, outlined earlier in Section 2, of how a hydrogen atom, initially trapped in an oxygen vacancy site, can be brought onto an adjacent similar site. Practical calculations have been done according to NEB formalism implemented in QE code; comparison of results obtained with 13 and with 25 images along the path gives us credibility regarding the barrier height, whereby the barrier profile obtained with 25 images is more smooth and permits us to discuss some details. All the paths must, in principle, be left−right symmetric; this is not exactly the case for paths 4 and 5, due to numerical "noise" in the course of practical NEB calculations. From the end points, the energy profile departs nicely parabolically, which is not so obvious with 13 images but much better represented for a 25-images path (cf. bottom right panel in Figure 8). Assuming that the hydrogen atom vibrates *alone* around its equilibrium position at the extremity of each path, the corresponding frequency from fitting the corresponding force constant falls between 776 cm^{-1} (along the path 4 or 5) and 816 cm^{-1} (along the path 3). This nicely matches the prediction from the "full" phonon calculation addressed above.

We turn now to a discussion of different paths. The paths 4 and 5 seem degenerate; that follows indeed from an observation that the midpoint in each of them is the same, namely, a Ti vacancy site, from which the path can equally turn "downwards" or "upwards", consistently to drawings in the two last panels of Figure 1. One sees a shallow local minimum on top of the barrier, already mentioned in subsection 4.2 as a manifestation of magnetic solution. Therefore, this is a metastable position for a hydrogen atom, rather than a genuine saddle point. However, there is a subtlety. If the midpoint of path 5 is placed at the Ti vacancy site by the crystal symmetry, the midpoint of path 4 is subject to technical "drift", depending on the spring constant along the NEB, or other details of the algorithm used. As a result, the path may tend to get shortened by displacing its midpoint slightly "downwards" (closer to the oxygen atom, as is suggested by a drawing of path 4 in Figure 1), correspondingly climbing the midpoint energy upward. Such a "perturbation" would eventually destroy the local minimum on top of the barrier. This was not the case in our calculation which preserved the similarity of the energy profiles along path 4 and path 5. We note that the barrier height in corresponding NEB calculations, 3.71 eV, is expectedly close to the difference between previously discussed adsorption energies at the Ti vacancy and the O vacancy sites, i.e., +0.75 − (−2.87) = 3.62 eV. The mismatch of 0.09 eV may be attributed to the technical difference between the constraints imposed in the course of "conventional" conjugate-gradient search and in an NEB calculation. We emphasize that the profile of path 5 is an "improved version" of the energy profile preliminary scanned in a row of SIESTA calculations and depicted in Figure 5.

The "bottleneck" of paths 1 and 3 is the hydrogen atom squeezing through the intact Ti−O−Ti−O square face. The difference is that on the "upward" (see Figure 1) path 1 this face is within a (010) lattice plane, whereas for path 3 it makes a $(20\bar{1})$ plane. In path 2, the hydrogen atom passes through an incomplete square face, missing a Ti atom at one of its corners. The snapshots of the atomic relaxation within the corresponding planes is shown in Figure 9, in comparison with the unperturbed (no hydrogen) situation. One notes that, on passing through the "bottleneck", the hydrogen atom only slightly repels its Ti neighbors (Ti−Ti diagonal increases by ∼3%) but quite considerably (∼27% of the initial distance) pushes apart the O neighbors. This repulsion can be understood from purely electrostatic arguments, since hydrogen, like oxygen, is more electronegative than titanium and receives some electron density from the latter. For this reason, skirting an oxygen atom in the midpoint of path 4 does not bring this path considerably to the side (downward in Figure 1), as discussed above, whereas the path 2, laid in fact across a cavity with missing Ti atom, comes quite close to the remaining Ti atom, which the path skirts.

With the "bottlenecks" on path 1 and path 3 being so similar (cf. Figure 9), we cannot suggest any obvious reason for the difference in corresponding barrier heights other than the "natural" anisotropy of the crystal structure. In any case, path 2 undoubtedly possesses the lowest energy barrier, since it does not include a passage between closely placed two Ti and two O atoms, pushing those latter to the sides. Consequently, path 2 is expected to dominate among hypothetical channels of hydrogen diffusion, to which the other paths, possessing the barrier energy of the same order of magnitude, should contribute in parallel without being a priori excluded.

https://doi.org/10.1021/acs.jpcc.3c00750
J. Phys. Chem. C 2023, 127, 11787−11800

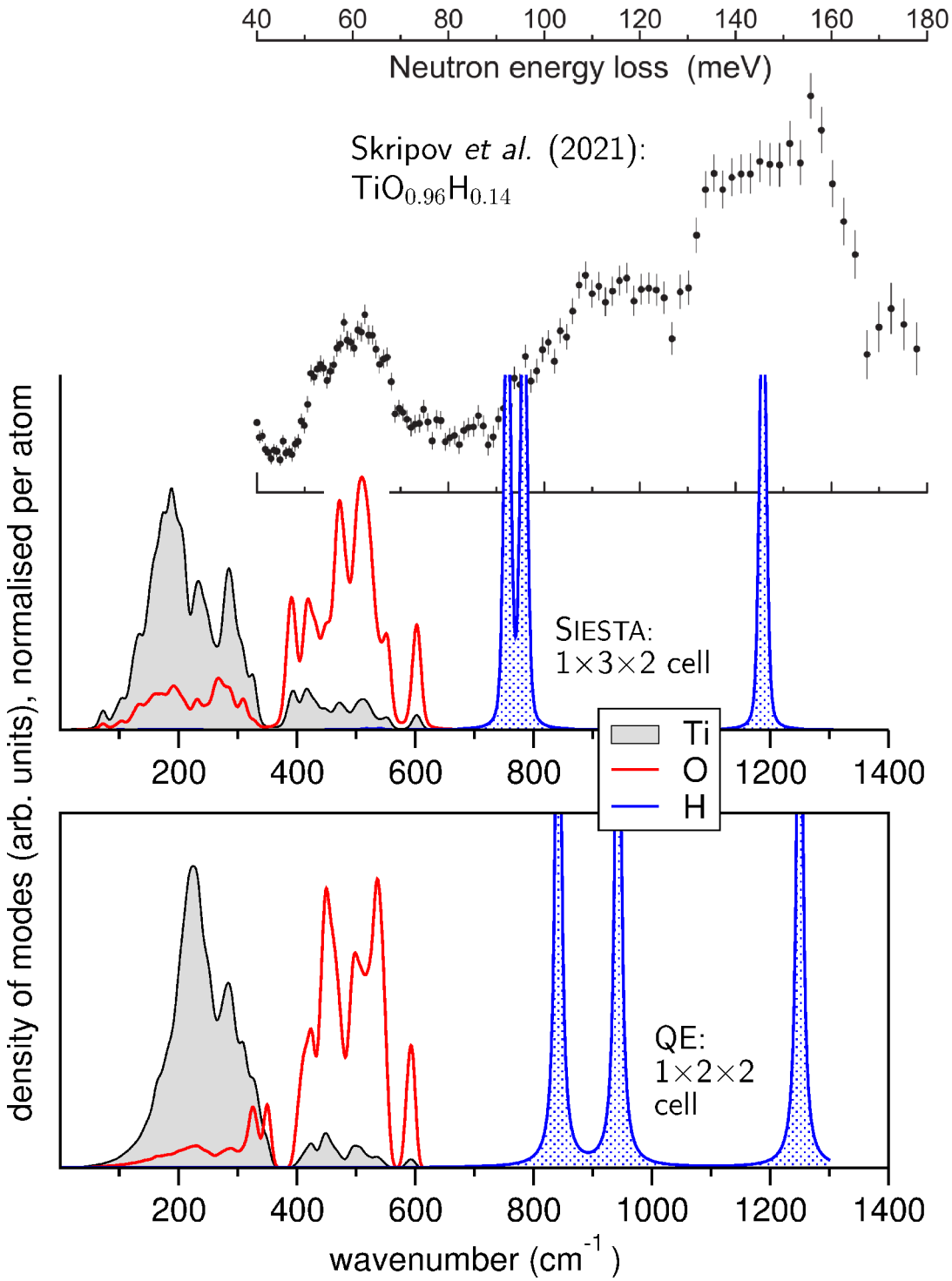

Figure 6. Densities of vibration modes of TiO with H occupying an oxygen vacancy site (one per supercell indicated), calculated by QE (bottom panel) and SIESTA (middle panel). Neutron scattering spectrum of monoclinic $TiO_{0.96}H_{0.14}$, shown for comparison in the upper panel, is reproduced from Figure 5 of ref 20. Copyright Elsevier (2021). See text for detail.

The height of the barrier measured from the end point minima, i.e., the activation energy E_a, may, in principle, serve to estimate the reaction (e.g., diffusion) rate D via the Arrhenius equation (see, e.g., the review by Gomer[50] for detail).

$$D = \nu \times \exp\left(-\frac{E_a}{k_B T}\right) \quad (2)$$

A more detailed analysis of different contributions to the flux of hydrogen atoms induced by gradient of concentrations and involving hoppings over the barriers was given by Kirchheim and Pundt,[48] culminating in eq (55) of their work. The frequency prefactor ν (called "attempt frequency" in ref 48) may vary in very broad ranges, depending on the reaction type; estimations for proton diffusion in TiO might be not obvious. Zhdanov[51] summarized a number of parameters from the literature in Tables 1 and 2 of his review work; for instance, for

https://doi.org/10.1021/acs.jpcc.3c00750
J. Phys. Chem. C 2023, 127, 11787−11800

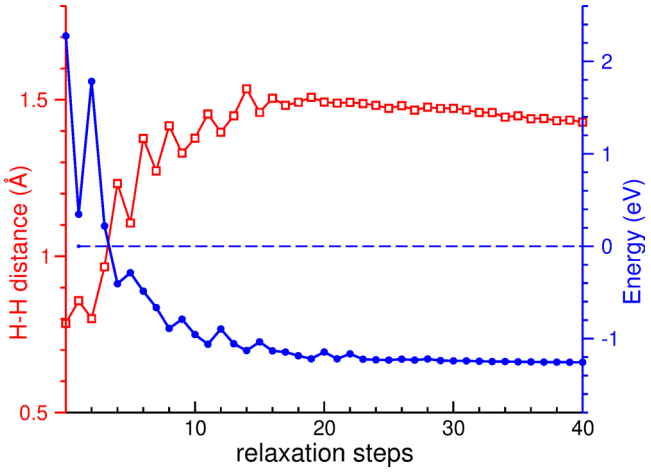

Figure 7. Evolution of interatomic distance (left scale, red squares) and total energy (right scale, blue dots) of an H_2 molecule placed in an oxygen vacancy, after a SIESTA calculation. Zero energy corresponds to a situation with a single H atom relaxed at an oxygen vacancy site and another one being free. See text for details.

desorption of H_2 from Pt ν makes 10^6 s^{-1} and from other different metal surfaces -10^{12} to 10^{17} s^{-1}. In any case, huge heights of the barriers relative to the ambient thermal energy (k_BT = 26 meV at 25 °C) in a practical sense identify the diffusion over barriers as an utterly improbable event. A general understanding is that quantum tunneling plays an important role in hydrogen transport in metals.[52,53] A more detailed analysis along this line would go beyond the scope of the present work, but it is likely to be responsible for much higher mobility of hydrogen in different materials than it could be understood in terms of hopping over the barriers. Coming back specifically to TiO, Skripov et al.[20] set ~10^5 s^{-1} as the upper limit on the hydrogen jump rate in strongly sub-stoichiometric and nearly stoichiometric H-doped TiO, referring to the NMR line width: "... H atoms in titanium monoxides appear to be immobile on the NMR frequency scale up to 370 K". As an explanation, Skripov et al. evoke spatial separation between the oxygen vacancy sites. We reinforce this conclusion by identifying barrier heights as unusually high, by the standards of hydrogen diffusion in metals. For comparison, Pozzo and Alfè[54] calculated the diffusion barriers for hydrogen atoms over the Mg(0001) surface doped with different transition metals to span the values from nearly zero (Ag doping) to—the largest among the systems probed—0.94 eV (Zr doping) and 0.75 eV (Ti doping).

In view of high barriers separating the hydrogen adsorption sites, and in agreement with the experimental evidence so far available, TiO seems to be promising for accumulating hydrogen, even if not so in terms of easiness of the hydrogen

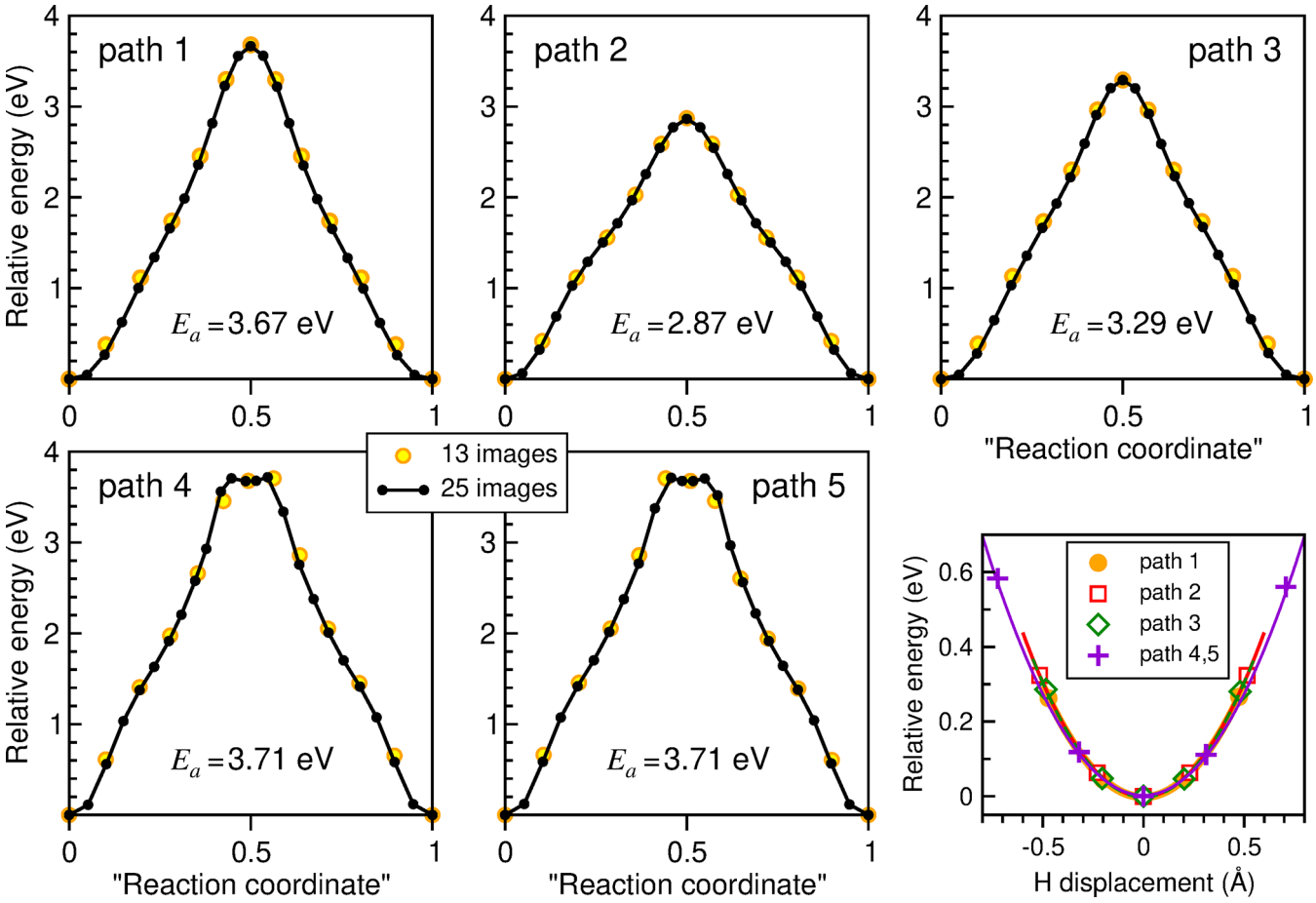

Figure 8. NEB energy profiles for H atom displacement along the five paths specified in Figure 1. Results of calculations performed with 13 and with 25 images along each path are shown for comparison. The barrier height is indicated for each path. In the bottom right panel, the total energy is traced as a function of absolute displacement of the hydrogen atom from the equilibrium position, near the beginning and the end of each path.

https://doi.org/10.1021/acs.jpcc.3c00750
J. Phys. Chem. C 2023, 127, 11787−11800

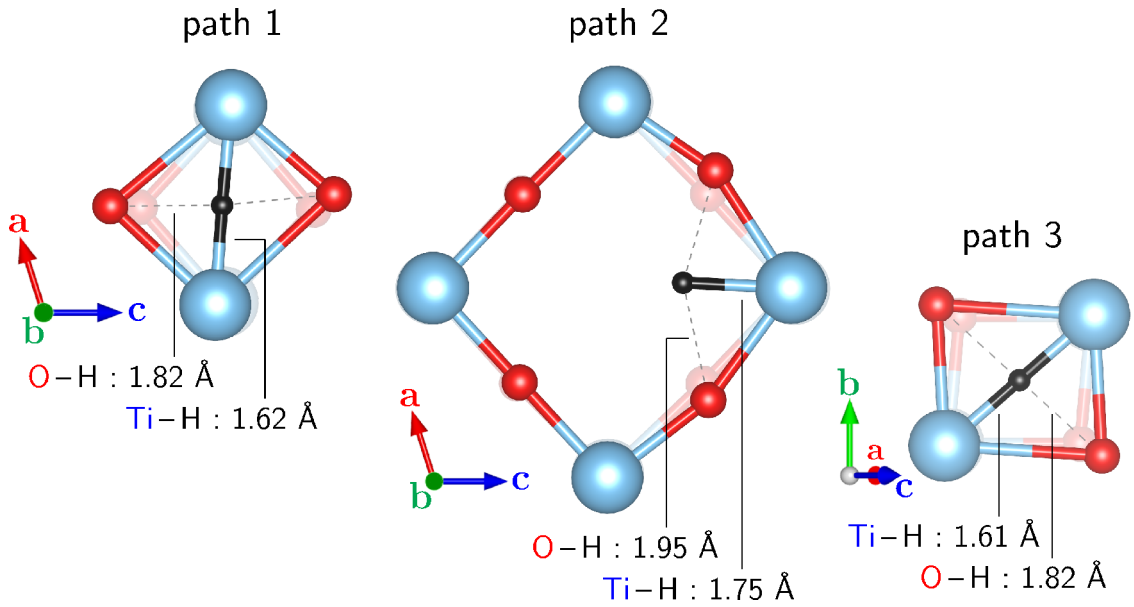

Figure 9. Optimized structures at the saddle points of paths 1, 2, and 3. Distances between the hydrogen atom and its nearest Ti and O neighbors are indicated. The corresponding equilibrium structures in the absence of hydrogen are shown faded in the background.

diffusion. This can give rise to interesting applications, with a perspective of extension over other related materials. Interestingly, the group of Lefort et al. reported[55,56] an enormous capacity to accommodate hydrogen (up to 2.9 wt. %) for highly sub-stoichiometric titanium carbide, $TiC_{0.6}$, which was not the case in weakly substoichiometric $TiC_{0.9}$. The authors attribute this property to the presence of long-range-ordered carbon vacancies in $TiC_{0.6}$, in contrast to $TiC_{0.9}$. In view of the similarity of the crystal structures of titanium carbide and monoxide, this discovery is stimulating for the extension of our present study.

5. CONCLUSIONS

Summarizing, we performed first-principles calculations of electronic structure, lattice vibrations, and possible diffusion barriers in monoclinic TiO doped with H atom. Our results reinforce the earlier available experimental evidence that hydrogen atoms enter the oxygen vacancy sites, the related energy gain now being estimated as ≃2.87 eV. Moreover, the Ti vacancy sites were identified as possible metastable positions for adsorbed hydrogen atoms, unfavorable in energy (with respect to the case of desorbed hydrogen) by 0.75 eV. The Ti vacancy site makes a midpoint of two possible diffusion paths (those with the highest barrier, 3.71 eV) connecting two adjacent O vacancy sites. The lowest-energy path (with the barrier height of 2.87 eV) goes around a Ti atom at a distance of 1.75 Å from it. Different paths involve squeezing the H atom through different crystal structure bottlenecks, whereby the O atoms are considerably pushed away and the Ti atoms are somehow attracted toward the hydrogen atom. The estimated values of barrier height are too high to account for an appreciable hydrogen diffusion rate, assuming the hoppings over barriers as the principal diffusion mechanism. It seems plausible that quantum tunneling processes may play an important role, as is the case with hydrogen diffusion in other materials. Calculations of a lattice vibration spectrum are consistent with earlier reported results of inelastic neutron diffusion; the remaining deviations offer a substance for discussion about the placement of hydrogen atoms within the oxygen-vacancy cages.

Under an angle of possible applications, our study demonstrates that (and explains why) the Ti monoxide may absorb a considerable amount of hydrogen, which however tends to remain immobile in the sense of diffusivity through the lattice. This might be promising, e.g., for superconductivity, the tendency for which can be addressed in a separate study. As another prospective extension toward practical needs, the uptake and dissociation of molecular hydrogen at the surface, an issue almost routinely simulated with some other materials, may seem interesting here. In the context of fundamental science, the manifestation of quantum effects in the uptake and diffusion of hydrogen may deserve a thorough study; moreover, an interplay of vacancy ordering and diffusion may happen to be interesting. In any case, an enrichment of experimental evidence will be highly motivating.

AUTHOR INFORMATION

Corresponding Author

Andrei Postnikov − *LCP-A2MC, Université de Lorraine, Metz F-57078 Cedex 3, France;* orcid.org/0000-0001-9203-6235; Phone: +33-372-749149; Email: andrei.postnikov@univ-lorraine.fr

Authors

S. Vahid Hosseini − *Superconductivity Research Laboratory (SRL), Department of Physics, University of Tehran, Tehran 14395-547, Iran; LCP-A2MC, Université de Lorraine, Metz F-57078 Cedex 3, France*

Mohammad Reza Mohammadizadeh − *Superconductivity Research Laboratory (SRL), Department of Physics, University of Tehran, Tehran 14395-547, Iran*

Complete contact information is available at: https://pubs.acs.org/10.1021/acs.jpcc.3c00750

Notes

The authors declare no competing financial interest.

https://doi.org/10.1021/acs.jpcc.3c00750
J. Phys. Chem. C 2023, 127, 11787−11800

■ ACKNOWLEDGMENTS

The authors thank Dr. Alexander Skripov for careful reading of the manuscript and for useful comments. The authors thank Elsevier for granting permission to reproduce Figure 5 from ref 20. S.V.H. and M.R.M. acknowledge partial financial support by the Research Council of the University of Tehran. S.V.H. and A.P. thank the mesocenter of calculation EXPLOR at the Université de Lorraine (Project 2019CPMXX0918) for granting access to computational resources.

■ REFERENCES

(1) Abe, J. O.; Popoola, A. P. I.; Ajenifuja, E.; Popoola, O. M. Hydrogen energy, economy and storage: Review and recommendation. *Int. J. Hydrogen Energy* **2019**, *44*, 15072−15086.
(2) Goodenough, J. B. Perspective on Engineering Transition-Metal Oxides. *Chem. Mater.* **2014**, *26*, 820−829.
(3) Sun, Y.; Zhang, T.; Li, C.; Xu, K.; Li, Y. Compositional engineering of sulfides, phosphides, carbides, nitrides, oxides, and hydroxides for water splitting. *J. Mater. Chem. A* **2020**, *8*, 13415−13436.
(4) Zhu, Y.; Lin, Q.; Zhong, Y.; Tahini, H. A.; Shao, Z.; Wang, H. Metal oxide-based materials as an emerging family of hydrogen evolution electrocatalysts. *Energy Environ. Sci.* **2020**, *13*, 3361−3392.
(5) Song, J.; Wei, C.; Huang, Z.-F.; Liu, C.; Zeng, L.; Wang, X.; Xu, Z. J. A review on fundamentals for designing oxygen evolution electrocatalysts. *Chem. Soc. Rev.* **2020**, *49*, 2196−2214.
(6) Shang, X.; Tang, J.-H.; Dong, B.; Sun, Y. Recent advances of nonprecious and bifunctional electrocatalysts for overall water splitting. *Sustainable Energy & Fuels* **2020**, *4*, 3211−3228.
(7) Burke, M. S.; Enman, L. J.; Batchellor, A. S.; Zou, S.; Boettcher, S. W. Oxygen Evolution Reaction Electrocatalysis on Transition Metal Oxides and (Oxy)hydroxides: Activity Trends and Design Principles. *Chem. Mater.* **2015**, *27*, 7549−7558.
(8) Wu, S.; Tseng, K.-Y.; Kato, R.; Wu, T.-S.; Large, A.; Peng, Y.-K.; Xiang, W.; Fang, H.; Mo, J.; Wilkinson, I.; et al. Rapid Interchangeable Hydrogen, Hydride, and Proton Species at the Interface of Transition Metal Atom on Oxide Surface. *J. Am. Chem. Soc.* **2021**, *143*, 9105−9112. PMID: 34047552
(9) Yoon, H.; Kim, Y.; Crumlin, E. J.; Lee, D.; Ihm, K.; Son, J. Direct Probing of Oxygen Loss from the Surface Lattice of Correlated Oxides during Hydrogen Spillover. *J. Phys. Chem. Lett.* **2019**, *10*, 7285−7292.
(10) Whittingham, M. S. Hydrogen motion in oxides: from insulators to bronzes. *Solid State Ionics* **2004**, *168*, 255−263. Proceedings of the Workshop on Hydrogen: Ionic, Atomic and Molecular Motion
(11) Nolan, H.; Browne, M. P. Hydrogen energy currency: Beyond state-of-the-art transition metal oxides for oxygen electrocatalysis. *Current Opinion in Electrochemistry* **2020**, *21*, 55−61.
(12) Oelerich, W.; Klassen, T.; Bormann, R. Metal oxides as catalysts for improved hydrogen sorption in nanocrystalline Mg-based materials. *J. Alloys Compd.* **2001**, *315*, 237−242.
(13) Oelerich, W.; Klassen, T.; Bormann, R. Hydrogen Sorption of Nanocrystalline Mg at Reduced Temperatures by Metal-Oxide Catalysts. *Adv. Eng. Mater.* **2001**, *3*, 487−490.
(14) Yin, X.-L.; Calatayud, M.; Qiu, H.; Wang, Y.; Birkner, A.; Minot, C.; Wöll, C. Diffusion versus Desorption: Complex Behavior of H Atoms on an Oxide Surface. *ChemPhysChem* **2008**, *9*, 253−256.
(15) Feng, H.; Xu, Z.; Ren, L.; Liu, C.; Zhuang, J.; Hu, Z.; Xu, X.; Chen, J.; Wang, J.; Hao, W.; et al. Activating Titania for Efficient Electrocatalysis by Vacancy Engineering. *ACS Catal.* **2018**, *8*, 4288−4293.
(16) Zhu, K.; Shi, F.; Zhu, X.; Yang, W. The roles of oxygen vacancies in electrocatalytic oxygen evolution reaction. *Nano Energy* **2020**, *73*, 104761.
(17) Hu, X.; Trudeau, M.; Antonelli, D. M. Hydrogen Storage in Microporous Titanium Oxides Reduced by Early Transition Metal Organometallic Sandwich Compounds. *Chem. Mater.* **2007**, *19*, 1388−1395.
(18) Li, Y.; Yu, Z. G.; Wang, L.; Weng, Y.; Tang, C. S.; Yin, X.; Han, K.; Wu, H.; Yu, X.; Wong, L. M.; et al. Electronic-reconstruction-enhanced hydrogen evolution catalysis in oxide polymorphs. *Nat. Commun.* **2019**, *10*, 3149.
(19) Swaminathan, J.; Subbiah, R.; Singaram, V. Defect-Rich Metallic Titania ($TiO_{1.23}$) − An Efficient Hydrogen Evolution Catalyst for Electrochemical Water Splitting. *ACS Catal.* **2016**, *6*, 2222−2229.
(20) Skripov, A. V.; Soloninin, A. V.; Valeeva, A. A.; Gusev, A. I.; Rempel, A. A.; Wu, H.; Udovic, T. J. Hydrogen in nonstoichiometric cubic titanium monoxides: X-ray and neutron diffraction, neutron vibrational spectroscopy and NMR studies. *J. Alloys Compd.* **2021**, *887*, 161353.
(21) Watanabe, D.; Castles, J. R.; Jostsons, A.; Malin, A. S. The ordered structure of TiO. *Acta Crystallogr.* **1967**, *23*, 307−313.
(22) Denker, S. P. Relation of bonding and electronic band structure to the creation of lattice vacancies in TiO. *J. Phys. Chem. Solids* **1964**, *25*, 1397−1405.
(23) Valeeva, A. A.; Rempel, A. A.; Müller, M. A.; Reichle, K. J.; Tang, G.; Sprengel, W.; Schaefer, H.-E. Identification of Atomic Vacancies in Titanium Monoxide by Electron Microdiffraction and Positron Annihilation. *physica status solidi (b)* **2001**, *224*, R1−R3.
(24) Banus, M. D.; Reed, T. B.; Strauss, A. J. Electrical and Magnetic Properties of TiO and VO. *Phys. Rev. B* **1972**, *5*, 2775−2784.
(25) Gusev, A. Niobium Monoxide Superstructures. *JETP Letters* **2020**, *111*, 176−182.
(26) Neckel, A.; Rastl, P.; Eibler, R.; Weinberger, P.; Schwarz, K. Results of self-consistent band-structure calculations for ScN, ScO, TiC, TiN, TiO, VC, VN and VO. *Journal of Physics C: Solid State Physics* **1976**, *9*, 579−592.
(27) Leung, C.; Weinert, M.; Allen, P. B.; Wentzcovitch, R. M. First-principles study of titanium oxides. *Phys. Rev. B* **1996**, *54*, 7857−7864.
(28) Andersson, D. A.; Korzhavyi, P. A.; Johansson, B. Thermodynamics of structural vacancies in titanium monoxide from first-principles calculations. *Phys. Rev. B* **2005**, *71*, 144101.
(29) Schoen, J. M.; Denker, S. P. Band Structure, Physical Properties, and Stability of TiO by the Augmented-Plane-Wave Virtual-Crystal Approximation. *Phys. Rev.* **1969**, *184*, 864−873.
(30) Graciani, J.; Márquez, A.; Sanz, J. F. Role of vacancies in the structural stability of α-TiO: A first-principles study based on density-functional calculations. *Phys. Rev. B* **2005**, *72*, 054117.
(31) Kostenko, M. G.; Lukoyanov, A. V.; Zhukov, V. P.; Rempel, A. A. Vacancies in ordered and disordered titanium monoxide: Mechanism of B1 structure stabilization. *J. Solid State Chem.* **2013**, *204*, 146−152.
(32) Kajita, S.; Minato, T.; Kato, H. S.; Kawai, M.; Nakayama, T. First-principles calculations of hydrogen diffusion on rutile TiO_2(110) surfaces. *J. Chem. Phys.* **2007**, *127*, 104709.
(33) Watanabe, D.; Castles, J. R.; Jostsons, A.; Malin, A. S. Ordered Structure of Titanium Oxide. *Nature* **1966**, *210*, 934.
(34) Perdew, J. P.; Burke, K.; Ernzerhof, M. Generalized Gradient Approximation Made Simple. *Phys. Rev. Lett.* **1996**, *77*, 3865−3868.
(35) Hu, Z.; Metiu, H. Choice of *U* for DFT+*U* Calculations for Totanium Oxides. *J. Chem. Phys.* **2011**, *115*, 5841−5845.
(36) Giannozzi, P.; Baroni, S.; Bonini, N.; Calandra, M.; Car, R.; Cavazzoni, C.; Ceresoli, D.; Chiarotti, G. L.; Cococcioni, M.; Dabo, I.; et al. Quantum ESPRESSO: a modular and open-source software project for quantum simulations of materials. *J. Phys.: Condens. Matter* **2009**, *21*, 395502.
(37) Giannozzi, P.; Andreussi, O.; Brumme, T.; Bunau, O.; Buongiorno Nardelli, M.; Calandra, M.; Car, R.; Cavazzoni, C.; Ceresoli, D.; Cococcioni, M.; et al. Advanced capabilities for materials modelling with Quantum ESPRESSO. *J. Phys.: Condens. Matter* **2017**, *29*, 465901.
(38) Soler, J. M.; Artacho, E.; Gale, J. D.; García, A.; Junquera, J.; Ordejón, P.; Sánchez-Portal, D. The SIESTA method for *ab initio* order-*N* materials simulation. *J. Phys.: Condens. Matter* **2002**, *14*, 2745.

https://doi.org/10.1021/acs.jpcc.3c00750
J. Phys. Chem. C 2023, 127, 11787−11800

(39) García, A.; Papior, N.; Akhtar, A.; Artacho, E.; Blum, V.; Bosoni, E.; Brandimarte, P.; Brandbyge, M.; Cerdá, J. I.; Corsetti, F.; et al. Siesta: Recent developments and applications. *J. Chem. Phys.* **2020**, *152*, 204108.
(40) Vanderbilt, D. Soft self-consistent pseudopotentials in a generalized eigenvalue formalism. *Phys. Rev. B* **1990**, *41*, 7892−7895.
(41) Troullier, N.; Martins, J. L. Efficient pseudopotentials for plane-wave calculations. *Phys. Rev. B* **1991**, *43*, 1993.
(42) Monkhorst, H. J.; Pack, J. D. Special points for Brillouin-zone integrations. *Phys. Rev. B* **1976**, *13*, 5188.
(43) van Duijneveldt, F. B.; van Duijneveldt-van de Rijdt, J. G. C. M.; van Lenthe, J. H. State of the Art in Counterpoise Theory. *Chem. Rev.* **1994**, *94*, 1873−1885.
(44) Sheppard, D.; Terrell, R.; Henkelman, G. Optimization methods for finding minimum energy paths. *J. Chem. Phys.* **2008**, *128*, 134106.
(45) Fujimori, A.; Tsuda, N. Electronic structure of non-stoichiometric titanium hydride. *Journal of the Less Common Metals* **1982**, *88*, 269−272.
(46) Smithson, H.; Marianetti, C. A.; Morgan, D.; Van der Ven, A.; Predith, A.; Ceder, G. First-principles study of the stability and electronic structure of metal hydrides. *Phys. Rev. B* **2002**, *66*, 144107.
(47) Barman, S. R.; Sarma, D. D. Electronic structure of TiO_x ($0.8 < x < 1.3$) with disordered and ordered vacancies. *Phys. Rev. B* **1994**, *49*, 16141−16148.
(48) Kirchheim, R.; Pundt, A. In *Physical Metallurgy*, 5th ed.; Laughlin, D. E., Hono, K., Eds.; Elsevier: Oxford, UK, 2014; pp 2597−2705.
(49) Mills, G.; Jónsson, H. Quantum and thermal effects in H_2 dissociative adsorption: Evaluation of free energy barriers in multidimensional quantum systems. *Phys. Rev. Lett.* **1994**, *72*, 1124−1127.
(50) Gomer, R. Diffusion of adsorbates on metal surfaces. *Rep. Prog. Phys.* **1990**, *53*, 917−1002.
(51) Zhdanov, V. P. Arrhenius parameters for rate processes on solid surfaces. *Surf. Sci. Rep.* **1991**, *12*, 185−242.
(52) Birnbaum, H. K.; Flynn, C. P. Hydrogen Tunneling States in Niobium. *Phys. Rev. Lett.* **1976**, *37*, 25−28.
(53) Kehr, K. W. In *Hydrogen in Metals I: Basic Properties;* Alefeld, G., Völkl, J., Eds.; Springer Berlin Heidelberg: Berlin, Germany, 1978; pp 197−226.
(54) Pozzo, M.; Alfè, D. Hydrogen dissociation and diffusion on transition metal (=Ti, Zr, V, Fe, Ru, Co, Rh, Ni, Pd, Cu, Ag)-doped Mg(0001) surfaces. *Int. J. Hydrogen Energy* **2009**, *34*, 1922−1930.
(55) Gringoz, A.; Glandut, N.; Valette, S. Electrochemical hydrogen storage in $TiC_{0.6}$, not in $TiC_{0.9}$. *Electrochem. Commun.* **2009**, *11*, 2044−2047.
(56) Nguyen, J.; Glandut, N.; Jaoul, C.; Lefort, P. Hydrogen insertion in substoichiometric titanium carbide. *Int. J. Hydrogen Energy* **2015**, *40*, 8562−8570.

https://doi.org/10.1021/acs.jpcc.3c00750
J. Phys. Chem. C 2023, 127, 11787−11800

P22

3/2 magic angle quantization rule of flat bands and its relationship to the quantum Hall effect and localization centers of the electronic wave functions at high order magic angles in twisted bilayer graphene

Leonardo A. Navarro-Labastida[1] **and Gerardo G. Naumis** [1]

[1]*Depto. de Sistemas Complejos, Instituto de Física, Universidad Nacional Autónoma de México (UNAM). Apdo. Postal 20-364, 01000, CDMX, México.*

Twisted bilayer graphene (TBG) is known for exhibiting highly correlated phases at magic angles due to the emergence of flat bands that enhance electron-electron interactions. The connection between magic angles and the Quantum Hall effect remains a topic of ongoing research. In the TBG chiral model [1], electronic wave function properties depend on a single parameter (α), inversely proportional to the relative twist angle between the two graphene layers and which includes the interlayer interaction strength. In previous studies, as the twist angles approached small values, strong confinement and a convergence to coherent Landau states were observed. However, the origin of these phenomena remained elusive. This work explores flat-band electronic modes, revealing that flat band states exhibit self-duality; they are coherent Landau states in reciprocal space. Subsequently, by symmetrizing the wave functions and considering the squared TBG Hamiltonian [2], the strong confinement observed in the limit of small twist angles is explained. This confinement arises from the combination of the symmetrized squared norm of the moiré potential and the quantized orbital motion of electrons, effectively creating a quantum well. The ground state of this well, located at defined spots, corresponds to Landau levels with energy determined by the magic angle. Furthermore, we demonstrate that the problem is physically analogous to an electron attached to a non-Abelian SU(2) gauge field with an underlying C3 symmetry. In regions of strong confinement, the system can be considered as Abelian, aligning with the picture of a simple harmonic oscillator. This allows to define a magnetic energy in which the important role of the wave function parity and gap closing at non-magic angles is revealed. Finally, we investigate the transition from the original non-Abelian nature to an Abelian state by artificially changing the pseudo-magnetic vector components from an SU(2) to a U(1) field, which alters the sequence of magic angles.

[1] G. Tarnopolsky, A. J. Kruchkov, and A. Vishwanath, Phys. Rev. Lett. 122, 106405 (2019).
[2] L. A. Navarro-Labastida and G. G. Naumis, Phys. Rev. B 107, 155428 (2023).

P23

Exciton-polaritons in an one-dimensional hexagonal boron nitride superlattice

P. Ninhos[1], **N.M.R. Peres**[1,2], **N.A. Mortensen**[1], **C. Tserkezis**[1]

[1] *POLIMA, University of Southern Denmark, Odense, Denmark*
[2] *Department and Centre of Physics, University of Minho, Braga, Portugal*

Since the discovery of graphene and its unusual electronic properties, two-dimensional (2D) materials have been stimulating the curiosity of the scientific community and have become a key research topic of general interest. Of particular relevance is monolayer hexagonal boron nitride (that we will denote simply by hBN), a semiconductor that displays an intense absorption in the ultraviolet range. This fact deems it promising for the development of sensors of biomolecules that have an intense absorption in the same spectral range, such as the cyclic beta-helical peptides. Due to the reduced thickness of 2D materials, they show a reduced dielectric screening, which makes it possible for formation of excitons at room temperature, and bigger excitonic binding energies compared to conventional semiconductors.

Studies on the sub-gap optical properties of hBN can be found in the literature [1, 2], but there is the need for ways of controlling the excitonic properties of hBN. In this work, we suggest a form of tuning the excitonic binding energies by applying a one-dimensional periodic potential on top of hBN. In this way, we form a semiconducting superlattice structure that has distinct electronic properties from the original lattice. Namely, introducing the one-dimensional potential leads to the renormalization of the gap and of the Fermi velocity along the direction perpendicular to the potential [3]. This deems the low-energy dispersion anisotropic and to the renormalization of the electron and hole effective masses.

In this work, we have seen that increasing the period of the potential increases the anisotropy of the dispersion, which results in the red-shift of the excitonic levels. We computed as well the optical conductivity, and have observed that the intensity of the peaks in the conductivity increases as the frequency of the peaks red-shift.

Finally, we determine the dispersion relation of the polaritonic modes, i.e., confined light-matter hybrid modes that arise from excitations of polarizable media. In our case, the excitons are the origin of the polarization, so we call these modes exciton-polaritons. Our results show that as the period of the potential increases and the energies of the excitonic states red-shift, the exciton-polaritons become less confined.

[1] J. C. G. Henriques, G. B. Ventura, C. D. M. Fernandes, and N. M. R. Peres, J. Phys.: Condens. Matter, **32**, 025304 (2019).
[2] M. F. C. M. Quintela, J. C. G. Henriques, L.G.M. Tenório, and N. M. R. Peres, Phys. Stat. Sol. B, **259**, 2200097 (2022).
[3] C. H. Park, L. Yang, Y. W. Son, M. L. Cohen, and S. G. Louie, Phys. Rev. Lett., **101**, 126804 (2008).

P24

Electronic properties of twisted TMDs using Wannier based Tight-Binding model

G.Parra-Martínez [1] , J.A. Silva−Guillén [1] , and F.Guinea [1,2]

[1]Instituto Madrileño de Estudios Avanzados en Nanociencia (IMDEA-Nanociencia), Madrid, Spain

[2] Donostia International Physics Center, Paseo Manuel de Lardizabal 4, 20018 San Sebastian, Spain

Twisted homobilayer transition metal dichalcogenides have proven to be a unique platform to study a pletora of quantum states as experiments have found plenty of correlated physics, from chern insulators to fractional quantum anomalous hall states [1].
These systems display narrow valence bands that arise due to the moire pattern. These bands can host non trivial topology which can undergo topological phase transition as a function of the twist angle and perpendicular electric fields.
Here, we aim to understand the nature of some electronic behaviours of this class of materials using a wannier-based tight binding model [2] in order to include electronic correlations.
Due to the non-trivial topology of the system we need to select a set of bands with total chern number zero. We do so for the first three valence bands and constraint the gauge to center the Wannier orbitals at the high symmetry point of the moire superlattice. Following [2] we set the orbitals to be also polarized in the top and bottom layers.

[1] Cai, J. et al. 10.1038/s41586-023-06289-w, Nature (2023)
[2] Fengcheng Wu et al. arXiv:2305.01006 (2023)
[3] A. H. MacDonald Phys. Rev. Lett. 122, 086402 (2019)
[4] Das Sarma et al. Phys. Rev. Research 2, 033087 (2020)

P25

Non-local correlations and exciton condensation in a model Quantum Spin Hall Insulator

I. Pasqua[1] **and M. Fabrizio**[1]

[1] *International School for Advanced Studies (SISSA), Via Bonomea 265, I-34136 Trieste, Italy*

In the last years an increasing effort has been devoted to study the role of topology beyond the non-interacting picture. The interplay between topology and correlations in strongly interacting systems is very hard to tackle and yet not well understood.
Here we consider a model for a Quantum Spin Hall Insulator [1] (QSHI) and we add an on site Coulomb repulsion between the electrons. The phase diagram depicted by single-site DMFT [2] shows that the correlations give rise to a phase characterized by an excitonic condensation at the boundary between the QSHI and a Mott Insulator (MI).
In our work we go beyond single-site DMFT with its cluster extension, the Dynamical Cluster Approximation (DCA), and we investigate the role of the non-local correlations on the phase-diagram. We find that an excitonic phase between the QSHI and the MI is still present with renormalized phase boundaries. Furthermore this extension allows assessing whether the excitons in the Mott Insulator, which get soft and condense in the excitonic insulator, may be regarded as bound states of the valence and conduction bands of Green's function zeros.

[1] B. Bernevig, T. Houges and SC Zhang, Science **314**, 5806 (2006).
[2] A. Amaricci, G. Mazza, M. Capone and M. Fabrizio, PRB **107**, 115117 (2023).

P26

Effects of lattice relaxation on magnetism in twisted bilayer Moiré systems from first-principles

Aditya Putatunda & Sergey Artyukhin
Istituto Italiano di Tecnologia
Via Morego 30, Genova, 16123, Italy

Twisted bilayer structures of van der Waals materials attract great interest because of recent experimental advances in single layer exfoliation and processing allowed the discovery of a variety of correlated states[1,2]. Magnetic twisted bilayers hosting skyrmions have also been recently demonstrated. Since magnetic interactions are sensitive to interionic distances, to reproduce the experiments reliably, the crystal structure has to be well optimized, in order to include ionic relaxation effects. Within first-principles approach, large supercells and tight convergence are required to compute the magnetic interactions. Here we combine first-principles DFT and model simulations using Wannier function based tight-binding Hamiltonian to study the states in the twisted bilayer of CrI_3.

[1] Xu et al., Nature Nanotechnology 17, 143–147 (2022)
[2] N. Sivadas., Nano Lett. 18, 7658–7664 (2018)

P27

Dynamical correlations and order in magic-angle twisted bilayer graphene

Gautam Rai[1], **Lorenzo Crippa**[2], **Dumitru Călugăru**[3], **Haoyu Hu**[4], **Luca de' Medici**[5], **Antoine Georges**[6,7,8,9], **B. Andrei Bernevig**[3,4,10], **Roser Valentí**[11], **Giorgio Sangiovanni**[2], **Tim Wehling**[1,12]

[1] *I. Institute of Theoretical Physics, University of Hamburg, Notkestrasse 9, 22607 Hamburg, Germany*

[2] *Institut für Theoretische Physik und Astrophysik and Würzburg-Dresden Cluster of Excellence ct.qmat, Universität Würzburg, 97074 Würzburg, Germany*

[3] *Department of Physics, Princeton University, Princeton, New Jersey 08544, USA*

[4] *Donostia International Physics Center, P. Manuel de Lardizabal 4, 20018 Donostia-San Sebastian, Spain*

[5] *LPEM, ESPCI Paris, PSL Research University, CNRS, Sorbonne Université, 75005 Paris France*

[6] *Collège de France, Université PSL, 11 place Marcelin Berthelot, 75005 Paris, France*

[7] *Center for Computational Quantum Physics, Flatiron Institute, 162 Fifth Avenue, New York, New York 10010, USA*

[8] *Centre de Physique Théorique, Ecole Polytechnique, CNRS, Institut Polytechnique de Paris, 91128 Palaiseau Cedex, France*

[9] *DQMP, Université de Genève, 24 quai Ernest Ansermet, CH-1211 Genève, Suisse*

[10] *IKERBASQUE, Basque Foundation for Science, Bilbao, Spain*

[11] *Institut für Theoretische Physik, Goethe Universität Frankfurt, Max-von-Laue-Strasse 1, 60438 Frankfurt am Main, Germany*

[12] *The Hamburg Centre for Ultrafast Imaging, 22761 Hamburg, Germany*

The interplay of dynamical correlations and electronic ordering is pivotal in shaping phase diagrams of correlated quantum materials. In magic angle twisted bilayer graphene, transport, thermodynamic and spectroscopic experiments pinpoint at a competition between distinct low-energy states with and without electronic order, as well as a competition between localized and delocalized charge carriers. In our work [1,2], we utilize Dynamical Mean Field Theory (DMFT) on the topological heavy Fermion (THF) model of twisted bilayer graphene to investigate the emergence of electronic correlations and long-range order in the absence of strain. We explain the nature of emergent insulating and correlated metallic states, as well as transitions between them driven by three central phenomena: (i) the formation of local spin and valley isospin moments around 100K, (ii) the ordering of the local isospin moments around 10K, and (iii) a cascadic redistribution of charge between localized and delocalized electronic states upon doping. At integer fillings, we find that low energy spectral weight is depleted in the symmetric phase, while we find insulating states with gaps enhanced by exchange coupling in the zero-strain ordered phases. Doping away from integer filling results in distinct metallic states: a "bad metal" above the ordering temperature, where coherence of the low-energy electronic excitations is suppressed by scattering off the disordered local moments, and a "good metal" in the ordered states with coherence of quasiparticles facilitated by isospin order. Upon doping, there is charge transfer between the localized and delocalized orbitals of the THF model such that they get periodically filled and emptied in between integer fillings. This charge reshuffling manifests itself in cascades of doping-induced Lifshitz transitions, local spectral weight redistributions and periodic variations of the electronic compressibility ranging from nearly incompressible to negative. Our findings highlight the essential role of charge

transfer, hybridization and ordering in shaping the electronic excitations and thermodynamic properties in twisted bilayer graphene and provide a unified understanding of the most puzzling aspects of scanning tunneling spectroscopy, transport, and compressibility experiments.

[1] Gautam Rai, Lorenzo Crippa, Dumitru Călugăru, Haoyu Hu, Luca de' Medici, Antoine Georges, B. Andrei Bernevig, Roser Valentí, Giorgio Sangiovanni, Tim Wehling, arXiv:2309.08529.

[2] Haoyu Hu, Gautam Rai, Lorenzo Crippa, Jonah Herzog-Arbeitman, Dumitru Călugăru, Tim Wehling, Giorgio Sangiovanni, Roser Valenti, Alexei M. Tsvelik, B. Andrei Bernevig, arXiv:2301.04673 (Accepted PRL 2023).

P28

Mirror-protected Majorana zero modes in *f*-wave multilayer graphene superconductors

Võ Tiến Phong [1], Héctor Sainz-Cruz[2], Eugene J. Mele[1], and Francisco Guinea [2, 3]

[1] *Department of Physics and Astronomy, University of Pennsylvania, Philadelphia PA 19104, U.S.A*

[2] *IMDEA Nanoscience, Faraday 9, 28049 Madrid, Spain*

[3] *Donostia International Physics Center, Paseo Manuel de Lardizábal 4, 20018 San Sebastián, Spain*

Due to their non-Abelian braiding statistics and immunity to quantum decoherence, Majorana zero modes (MZMs) are highly sought after as building blocks for topological quantum computation [1-3]. Recent experiments have discovered superconductivity in chirally-stacked and twisted multilayer graphene [4-9]. In these materials, valley-odd *f*-wave pairing is emerging as a leading candidate for the superconducting symmetry [10-13]. Inspired by these developments, we study models of *f*-wave superconductivity on the honeycomb lattice with arbitrary numbers of layers. These models respect a mirror symmetry that allows classification of the bands by a mirror-projected winding number $\nu_{\pm}$. For odd numbers of layers, the systems are topologically non-trivial with $\nu_{\pm} = \pm 1$. Along each mirror-preserving edge in armchair nanoribbons, there are two protected Majorana zero modes. These modes are present even if the sample is finite in both directions, such as in rectangular and hexagonal flakes. Crucially, zero modes can also be confined to vortex cores, which can be created by a magnetic field or localized magnetic impurities and accessed by local scanning probes. Finally, we apply these models to twisted bilayer and trilayer systems, which also feature boundary-projected and vortex-confined zero modes, as shown Fig. 1. Since vortices are experimentally accessible [15-16], our study suggests that superconducting multilayer graphene systems are promising platforms to create and manipulate Majorana zero modes.

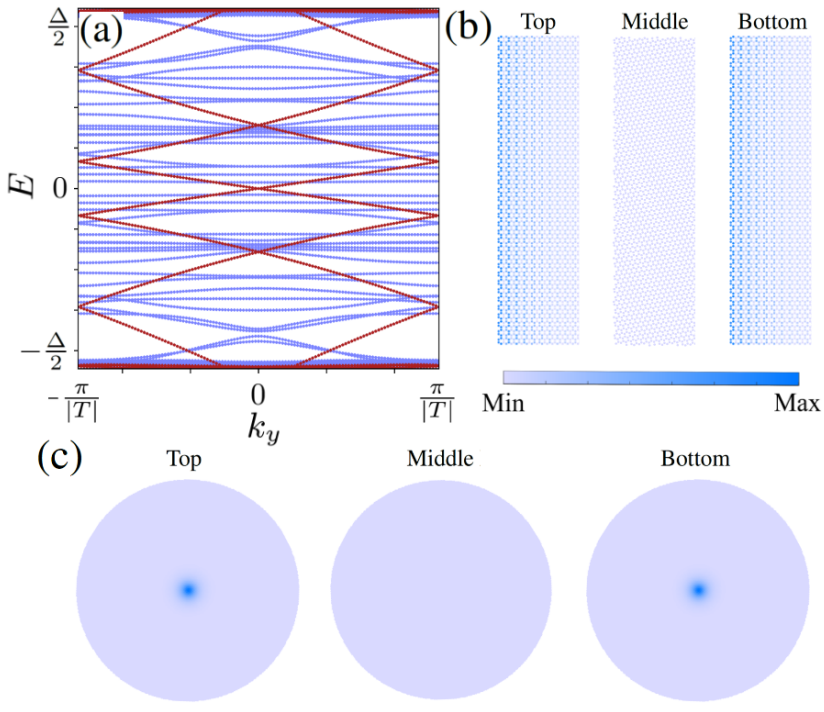

Figure 1 (a) Band structure of a twisted trilayer graphene nanoribbon with armchair edges in the top and bottom layers. The states in red come from the effective monolayer sector that results from the odd combination of top and bottom layers [14], so they have all the charge in these layers. (b) Charge map of a TTG zero mode at zero momentum in each of the three layers near the left edge of the ribbon. (f) Zero mode confined to a vortex core in twisted trilayer graphene, with $E \approx 10^{-10}$ eV.

[1] Ivanov, Dmitri A. "Non-Abelian statistics of half-quantum vortices in p-wave superconductors." *Physical review letters* 86, no. 2: 268. (2001).

[2] Kitaev, A. Yu. "Fault-tolerant quantum computation by anyons." *Annals of physics* 303, no. 1: 2-30. (2003).

[3] Nayak, Chetan, Steven H. Simon, Ady Stern, Michael Freedman, and Sankar Das Sarma. "Non-Abelian anyons and topological quantum computation." *Reviews of Modern Physics* 80, no. 3: 1083. (2008).

[4] Cao, Yuan, Valla Fatemi, Shiang Fang, Kenji Watanabe, Takashi Taniguchi, Efthimios Kaxiras, and Pablo Jarillo-Herrero. "Unconventional superconductivity in magic-angle graphene superlattices." *Nature* 556, no. 7699: 43-50. (2018).

[5] Park, Jeong Min, Yuan Cao, Kenji Watanabe, Takashi Taniguchi, and Pablo Jarillo-Herrero. "Tunable strongly coupled superconductivity in magic-angle twisted trilayer graphene." *Nature* 590, no. 7845: 249-255. (2021).

[6] Hao, Zeyu, A. M. Zimmerman, Patrick Ledwith, Eslam Khalaf, Danial Haie Najafabadi, Kenji Watanabe, Takashi Taniguchi, Ashvin Vishwanath, and Philip Kim. "Electric field–tunable superconductivity in alternating-twist magic-angle trilayer graphene." *Science* 371, no. 6534: 1133-1138. (2021).

[7] Zhang, Yiran, Robert Polski, Cyprian Lewandowski, Alex Thomson, Yang Peng, Youngjoon Choi, Hyunjin Kim et al. "Promotion of superconductivity in magic-angle graphene multilayers." *Science* 377, no. 6614: 1538-1543. (2022).

[8] Zhou, Haoxin, Tian Xie, Takashi Taniguchi, Kenji Watanabe, and Andrea F. Young. "Superconductivity in rhombohedral trilayer graphene." *Nature* 598, no. 7881: 434-438. (2021).

[9] Zhou, Haoxin, Ludwig Holleis, Yu Saito, Liam Cohen, William Huynh, Caitlin L. Patterson, Fangyuan Yang, Takashi Taniguchi, Kenji Watanabe, and Andrea F. Young. "Isospin magnetism and spin-polarized superconductivity in Bernal bilayer graphene." *Science* 375, no. 6582: 774-778. (2022).

[10] Oh, Myungchul, Kevin P. Nuckolls, Dillon Wong, Ryan L. Lee, Xiaomeng Liu, Kenji Watanabe, Takashi Taniguchi, and Ali Yazdani. "Evidence for unconventional superconductivity in twisted bilayer graphene." *Nature* 600, no. 7888: 240-245. (2021).

[11] Kim, Hyunjin, Youngjoon Choi, Cyprian Lewandowski, Alex Thomson, Yiran Zhang, Robert Polski, Kenji Watanabe, Takashi Taniguchi, Jason Alicea, and Stevan Nadj-Perge. "Evidence for unconventional superconductivity in twisted trilayer graphene." *Nature* 606, no. 7914: 494-500. (2022).

[12] Sainz-Cruz, Héctor, Pierre A. Pantaleón, Võ Tiến Phong, Alejandro Jimeno-Pozo, and Francisco Guinea. "Junctions and superconducting symmetry in twisted bilayer graphene." *Physical Review Letters* 131, no. 1: 016003. (2023).

[13] Crépel, Valentin, Tommaso Cea, Liang Fu, and Francisco Guinea. "Unconventional superconductivity due to interband polarization." *Physical Review B* 105, no. 9: 094506. (2022).

[14] Khalaf, Eslam, Alex J. Kruchkov, Grigory Tarnopolsky, and Ashvin Vishwanath. "Magic angle hierarchy in twisted graphene multilayers." *Physical Review B* 100, no. 8: 085109. (2019).

[15] Ge, Jun-Yi, Vladimir N. Gladilin, Jacques Tempere, Cun Xue, Jozef T. Devreese, Joris Van de Vondel, Youhe Zhou, and Victor V. Moshchalkov. "Nanoscale assembly of superconducting vortices with scanning tunnelling microscope tip." *Nature communications* 7, no. 1 (2016): 13880.

[16] Polshyn, Hryhoriy, Tyler Naibert, and Raffi Budakian. "Manipulating multivortex states in superconducting structures." *Nano letters* 19, no. 8 (2019): 5476-5482.

P29

Proximity-induced topological phases in a twisted heterostructure of transition metal dichalcogenide and CrI_3

Muzamil Shah and Gao Xianlong

Department of Physics, Zhejiang Normal University,Jinhua, Zhejiang Province, 321004, China

Depositing twisted heterostructure of transition metal dichalcogenide and CrI_3 has attracted huge attention as a novel way of tailoring 2D materials properties. In this work, we derive analytical expressions for the band structure of the twisted heterostructure of transition metal dichalcogenide and CrI_3 utilizing the proximity effects in the presence of an applied off-resonant optical field. We show that the proximity exchange in TMDCs due to ferromagnetic monolayer CrI_3 can be tuned by twisting. We investigate various topological quantum phases of the twisted heterostructure of transition metal dichalcogenide and CrI_3, when subject to an irradiated by off-resonant light field. We also calculate analytical expressions for orbital magnetization, the thermal and Nernst conductivities in different topological phases.

P30

Moiré-driven depinning and emerging chirality in twisting crystalline interfaces

Andrea Silva[1,3], Xin Cao[2], Xiang Gao[6], Emanuele Panizon[2,5], Melisa Gianetti[4], Roberto Guerra[4], Nicola Manini[4], Oded Hod[6], Michael Urbakh[6], Clemens Bechinger[2], Erio Tosatti[1,3,5], Andrea Vanossi[1,3]

[1]CNR-IOM, Via Bonomea 265, 34136 Trieste, Italy
[2]University Konstanz, 78464 Konstanz, Germany
[3]International School for Advanced Studies (SISSA), Via Bonomea 265, 34136 Trieste, Italy
[4]Università degli Studi di Milano, Via Celoria 16, 20133 Milano, Italy
[5]International Centre for Theoretical Physics (ICTP), Strada Costiera 11, 34151 Trieste, Italy
[6]Tel-Aviv University, Tel-Aviv 69978, Israel

In recent years, moiré materials gained attention due to their correlated-electrons behaviour, intimately linked to the distinctive moiré pattern arising from the mismatch and misalignment between two crystalline interfaces. While renowned for the exotic quantum phenomena they harbour, the mechanical properties of these moiré materials are less known, despite the fundamental role they play in the assembly and expected lifetime of twsitronic devices. We experimentally and theoretically study the rotational depinning and orientational dynamics of moiré materials in a versatile toy system of colloidal clusters on periodically corrugated surfaces in the presence of exerted torques imposed by means of a magnetic field [1].

The movement of 2D colloid lattices on the periodic substrate implies the evolution, with shrinkings and expansions, of the moiré pattern with the substrate. We demonstrate that the rotational depinning is controlled by the traversing of locally incommensurate (i.e. energetically less favorable) areas of the moiré pattern through the edges of clusters, which is hindered by potential barriers during cluster rotation. Our analytical model rationalises the depinning threshold as a function of cluster size. We demonstrate a striking collapse onto a universal curve, further revealing a cluster-size-independent rotation-translation depinning transition when lattice-matched clusters are driven jointly by a torque and a force.

The resulting design guidelines for twistronic devices are benchmarked in silico in a realistic atomistic contact of a graphitic flake over an *h*-BN substrate, where the elasticity of the contact leads to the emergence of a chiral deformation pattern.

[1] X. Cao, A. Silva, E. Panizon, A. Vanossi, N. Manini, E. Tosatti, C. Bechinger, Phys. Rev. X **12**, 021059 (2022).

P31

Defect-driven tunable electronic and optical properties of two-dimensional silicon carbide

Arushi Singh [1], Vikram Mahamiya [1,2] , and Alok Shukla [1]

[1] *Department of Physics, Indian Institute of Technology Bombay, Powai, Mumbai 400076, India*

[2] *National Institute for Materials Science (NIMS), 1-1 Namiki, Tsukuba, Ibaraki 305-0044, Japan*

Recently, an atomic scale two-dimensional silicon carbide monolayer has been synthesized [1] which opens up new possibilities for developing next-generation electronic and optoelectronic devices. Our study predicts the pristine SiC monolayer to have an “indirect” band gap of 3.38 eV (K→M) and a “direct” band gap of 3.43 eV (K→K) calculated using HSE06 functional. We performed a detailed investigation of the various possible defects (i.e., vacancies, foreign impurities, antisites, and their various combinations) on the structural stability, electronic, and optical properties of the SiC monolayer using a first-principles-based density-functional theory (DFT) and molecular dynamics (MD) simulations. A number of physical quantities such as the formation energy, electronic band gap, and the effective masses of charge carriers, have been calculated. We report that the SiC monolayer has a very low formation energy of 0.57 eV and can be stabilized upon TaC {111} film by performing the surface slab energy and interfacial adhesion energy calculations. Nitrogen doping is predicted to be the most favorable defect in silicon carbide monolayer due to its very low formation energy, indicating high thermodynamic stability. The analysis of the electronic band structure and the density of states shows that the additional impurity states are generated within the forbidden region in the presence of defects, leading to a significant reduction in the band gap. An interesting transition from semiconducting to metallic state is observed for N_C and Al_{Si} defective systems. For the pristine SiC monolayer, we find that the conduction band is nearly flat in the M→K direction, leading to a high effective mass of $3.48m_o$. A significant red shift in the absorption edge, as well as the occurrence of additional absorption peaks due to the defects, have been observed in the lower energy range of the spectrum. The calculated absorption spectra span over the visible and ultraviolet regions in the presence of defects, indicating that the defective SiC monolayers can have potential optoelectronic applications in the UV-vis region.

[1] C. M. Polley, H. Fedderwitz, T. Balasubramanian, A. A. Zakharov, R. Yakimova, O. Bäcke, J. Ekman, S. P. Dash, S. Kubatkin, and S. Lara-Avila, Phys. Rev. Lett. 130, 076203 (2023)

P32

Graphene striped moiré for 1D confinement and selective diffusion of metal atoms

Srdjan Stavrić [1,2,3] , Valeria Chesnyak[3,4], Simone del Puppo[3], Mirco Panighel[4], Giovanni Comelli[3,4], Cristina Africh[4], Željko Šljivančanin[2], Maria Peressi[3,5]

[1]Consiglio Nazionale delle Ricerche CNR-SPIN, c/o Università degli Studi "G. D'Annunzio", 66100 Chieti, Italy

[2] Vinča Institute of Nuclear Sciences - National Institute of the Republic of Serbia, University of Belgrade, P.O. Box 522, RS-11001 Belgrade, Serbia

[3]Physics Department, University of Trieste, via A. Valerio 2, 34127 Trieste, Italy

[4]CNR-IOM, Laboratorio TASC, S.S. 14 Km 163.5, Basovizza, 34149 Trieste, Italy

[5]ICSC - Italian Research Center on High Performance Computing, Big Data and Quantum Computing, Via Magnanelli 2, 40033 Casalecchio di Reno (BO), Italy

Graphene grown on hexagonal substrates with a lattice mismatch such as Ir(111) forms a hexagonal moiré pattern, that is used for self-assembly of well-ordered superlattices of transition metal clusters [1] and even single-atom magnets [2]. On the other hand, graphene grown on the Ni(100) surface, that has a square lattice, forms a distinct striped moiré pattern featuring valleys, where graphene strongly interacts with the nickel substrate, and ridges, where graphene exhibits a nearly free-standing behavior. Employing a combination of density functional theory (DFT) calculations and scanning tunneling microscopy (STM) measurements, we elucidate that this unique moiré pattern acts as a nanostructured template on a 2D support [1]. Within this framework, single metal atoms and small atomic clusters align along one-dimensional trails. DFT calculations reveal a selective and species-dependent confinment of metallic adsorbates. Notably, Co and Au exhibit opposing behaviors, as predicted by DFT and observed through STM. This discrepancy is attributed to the electrostatic interaction between the charged adsorbate and the nickel surface. Furthermore, this selectivity persists during the adsorbate's diffusion, resulting in unidirectional mass transport on a continuous 2D support. Our findings offer promising prospects for utilizing tailored nanostructured templates in various applications involving element-specific routes for mass transport.

[1] S. Stavrić, V. Chesnyak, S. del Puppo, M. Panighel, G. Comelli, C. Africh, Ž. Šljivančanin, M. Peressi, Carbon **215**, 118486 (2023).

[2] A. T. N'Diaye, S. Bleikamp, P. J. Feibelman, T. Michely, Phys. Rev. Lett. **97**, 215501 (2006)

[3] M. Pivetta, S. Rusponi, H. Brune, Phys. Rev. B **98**, 115417 (2018)

P33

Stabilizing the inverted phase of a WSe_2/BLG/WSe_2 heterostructure via hydrostatic pressure

Bálint Szentpéteri[1,2], Máté Kedves[1,2], Albin Márffy[1,3], Endre Tóvári[1,3], Nikos Papadopoulos[4], Prasanna K. Rout[4], Kenji Watanabe[5], Takashi Taniguchi[6], Srijit Goswami[4], Szabolcs Csonka[1,3], and Péter Makk[1,2]

[1] *Department of Physics, Institute of Physics, Budapest University of Technology and Economics, Műegyetem rkp. 3., H-1111 Budapest, Hungary*

[2] *MTA-BME Correlated van der Waals Structures Momentum Research Group, Műegyetem rkp. 3., H-1111 Budapest, Hungary*

[3] *MTA-BME Superconducting Nanoelectronics Momentum Research Group, Műegyetem rkp. 3., H-1111 Budapest, Hungary*

[4] *QuTech and Kavli Institute of Nanoscience, Delft University of Technology, 2600 GA Delft, The Netherlands*

[5] *Research Center for Functional Materials, National Institute for Materials Science, 1-1 Namiki, Tsukuba 305-0044, Japan*

[6] *International Center for Materials Nanoarchitectonics, National Institute for Materials Science, 1-1 Namiki, Tsukuba 305-0044, Japan*

To probe the interlayer interactions in van der Waals heterostructures, the pressure is an ideal tool, as it changes the interlayer distance and thus the interlayer tunneling.

Here, we show how the proximity induced spin-orbit coupling (SOC) is changed with the applied pressure in graphene and WSe_2 based devices. First, we show how the SOC is enhanced with weak anti- localization measurements [1]. Then, we also confirm the enhancement using the quantum Hall effect in bilayer graphene. Finally, we also show how the pressure can stabilize the inverted phase in a WSe2/bilayer graphene/WSe2 heterostructure. This phase occurs when the sign of the induced SOC is opposite for the top and bottom graphene layers [2].

[1] Fülöp, B., Márffy, A., Zihlmann, S. et al., npj 2D Mater Appl. **5**, 82 (2021).
[2] Kedves, M., et al., `arXiv:2303.12622`.